Modeling and Design of Controlled Flying Proximity Sliders for Head-Media Spacing Variation Suppression in Ultra-Low Flying Air Bearings

Jia-Yang Juang and David B. Bogy

Computer Mechanics Laboratory
Department of Mechanical Engineering
University of California at Berkeley
Berkeley, CA 94720

ABSTRACT

As the slider flying height (FH) continues to be reduced in hard disk drives, the flying height modulation (FHM) due to disk morphology and interface instability caused by highly nonlinear attractive forces becomes significant. Based on the concept that the FH of a portion of the slider that carries the read/write element can be adjusted by a piezoelectric actuator located between the slider and suspension and that the FH can be measured by use of a magnetic signal, a new 3-DOF analytic model and an observer-based nonlinear compensator are proposed to achieve ultra-low FH with minimum modulation under short range attractive forces. Numerical simulations show that the FHM due to disk waviness is effectively controlled and reduced.

1. INTRODUCTION

The areal density of magnetic recording in hard disk drives has been increasing at a rate of 1.6 times per year since the late 90's. This achievement has been enabled mechanically by decreasing the distance between the read/write transducer and the rotating disks. According to the Wallace spacing loss equation, the magnetic signal increases exponentially as the distance decreases between the magnetic media and the transducer. Therefore, the maximum magnetic signal can be potentially obtained at a spacing of zero, resulting in a contact recording scheme. However, when the slider comes into contact with the disk, other considerations must be addressed to assure a stable contact interface with minimum wear and contact bouncing vibration. Yanagisawa *et al.* [1] used a 0.3 mm diameter glass ball to study contact sliding experimentally and they showed that the wear of the spherical contact slider decreased as the gram load decreased, but the bouncing vibrations increased. In other words, there was a trade-off between reducing the bouncing and wear.

Ono *et al.* [2] numerically studied the effects of several parameters on the bouncing vibrations of a 1-DOF slider model and found that bouncing vibrations can be reduced by decreasing the contact stiffness and increasing the contact damping as well as applied load. Ono and Takahashi [3, 4] used a 2-DOF model for a tri-pad contact slider and showed that in order to achieve minimum bouncing it is necessary to design the contact pad such that its penetration depth is greater than the amplitude of the disk surface waviness. Such high penetration implies a relatively severe wear of the disk or slider. The effects of the front and rear air bearing stiffnesses, and the friction coefficient on the contact force and bouncing vibrations were analyzed numerically with a 2-DOF tri-pad slider model in Iida *et al.* [5]. It was found that the rear air bearing stiffness should be larger than the front air bearing

stiffness in order to reduce the vibration. However, contact forces may be increased if the rear air bearing is too stiff. Accordingly, there is an optimum rear air bearing stiffness in terms of both stable contact and wear durability.

In [6, 7], Ono and Iida used a 1-DOF model to investigate the design condition of a contact slider over a random wavy disk surface. Assuming a uniform contact pressure their simulation results showed that a larger contact pad area is better for wear durability because the contact stiffness and applied load necessary to attain contact sliding increases in proportion to the square root of the contact area. Asperity contact and bulk deformation were considered in Yamane *et al.* [8] to evaluate contact forces, contact stiffness, and contact pressure in the near-contact regime as a function of separation between the contact pad and disk surface. They showed that the mean contact force and spacing variation increased with an increase in the rms value of micro-waviness of the disk surface. The short range attractive forces between the slider and disk in the proximity regime have to be considered in both flying and contact sliders. These forces are strongly related to lubricant thickness, surface roughness, and slider/disk materials. More significant bouncing vibrations and flying height hysteresis have been observed experimentally when smoother disks or disks with a thicker lubricant are used.

Additionally, Iida and Ono [4, 5] included the meniscus attractive force in the random asperity contact simulations. They observed similar touch-down and take-off hysteresis as observed in experiments and showed that the attractive force could be significantly reduced if the rms value of asperity heights was increased or the asperity density was reduced. However, the attractive force increased with an increase in lubricant thickness. Yamane *et al.* [8] studied the bouncing vibration experimentally and by numerical simulation using a 2-

DOF dynamic model considering the adhesive force of the lubricant as well as the friction force. The frequency spectra of the trailing edge bouncing vibrations after touch-down and before take-off showed some similarity between experimental and numerical results but the vibration amplitudes had considerable disagreement between the two cases. The bouncing vibrations observed in the numerical simulations were self-excited vibrations caused by the combination effect of a relatively large short range attractive force and the friction force between the disk and slider when the contact occurred. These self-excited vibrations were negligible if the friction coefficient or the attractive force was small. The authors concluded that a contact slider with minimum self-excited bouncing can be achieved by use of a stiffer air bearing and with minimum friction coefficient and attractive force. Even though several design considerations have been proposed to design a contact slider in the literature, it is still unclear how those designs can be implemented into a real system, namely the design of the air bearing surface (ABS) and the selection of lubricants.

As the flying height (FH) is reduced in a flying head slider to the sub 3-nm regime in ultra-high density hard disk systems, the flying height modulation (FHM) induced by the disk morphology and dynamic instability due to short range attractive forces become more significant. Gupta and Bogy [9] conducted a numerical study on the effect of intermolecular and electrostatic forces on the stability of the HDI, and they showed that those short range attractive forces may cause an instability of the HDI at such low flying heights. This effect must be considered in the design of the ABS.

In order to achieve reliable reading and writing of magnetic data, it is required that the transducer location on the slider vibrate less than ±10% of the nominal FH, or about ±0.3 nm in future systems for 1 Tbit/in^2 areal density. Furthermore, considerable FHM may cause

instability of the interface due to adhesive forces. The concept of FH adjustment by piezoelectric material has been proposed in [10-12], but the main purpose was to decrease the effects of manufacturing tolerances and environmental variations on the FH. The authors utilized silicon microfabrication technology to fabricate the sliders. However, the use of silicon as the slider material may cause other issues in slider fabrication and HDI tribology. Li *et al.* [13] presented a real-time FH detection method by using readback or thermal signals and in [14] they developed a real-time feedback control method to suppress the FHM. In this case, the actuator was a piezoelectric film attached to the suspension. The actuation bandwidth was limited by the suspension dynamics. The effect of short range attractive forces was not taken into consideration in their study.

In this report, a novel controlled flying proximity (CFP) slider is presented. A new 3-DOF analytic model is proposed to describe the dynamics of the piezoelectric actuated slider. The air bearing parameters, such as stiffness and damping, are identified by a modal analysis method developed in the Computer Mechanics Laboratory (CML) [15, 16]. Then, an observer-based nonlinear sliding mode controller [17] is designed to compensate the short range attractive forces and to suppress the FHM of ultra-low flying height air-bearing sliders in proximity, in which the magnetic signal is used for real-time FHM measurement. The attractive forces are included in the model as a highly nonlinear term and the effect of disk morphology is modeled as unknown but bounded disturbances. The performance of the controller is investigated by numerical simulations.

2. NONLINEAR 3-DOF LUMPED PARAMETER MODEL OF CONTROLLED FLYING PROXIMITY (CFP) SLIDERS

The schematic diagram of the controlled flying proximity slider is shown in Fig. 1. The FH is about 20nm in the off duty cycle and is reduced to about 3nm during reading and writing. Figure 2 shows the five-pad ABS design example used in this report. The gap FH is adjusted by the deflection of the cantilever actuator. The deflection is achieved by grounding the slider and applying a negative voltage to the top electrode of the central piezoelectric material.

There are two modes of operation. In the passive mode, there is no external voltage applied to the piezoelectric material so the active cantilever rests in the original position. The gap flying height in this case may be designed to be anywhere between 10 and 20 nm, depending on the ABS design. In the active mode, the cantilever is bent into close proximity of the disk with the application of a negative DC voltage to the middle portion of the piezoelectric material. Meanwhile, an AC computed control voltage is superposed on the DC voltage so that the FHM is minimized. The active mode is used only when the read/write head is in operation. The duty cycle for a practical head is rather low. Most of the time of the head is spent on non-read/write actions, such as latency, seeking, or idle. Thus the wear and power consumption can be greatly reduced by simply operating the CFP in the passive mode. The air bearing pressure distributions in both modes are shown in Fig. 3, where the additional pressure peak is seen when the central pad is deflected into close proximity to the disk.

The CFP slider is modeled as a nonlinear 3-DOF lumped model in which the cantilever actuator and the air bearing dynamics are modeled as 1-DOF and 2-DOF, respectively.

2.1 1-DOF Lumped Model of the Piezoelectric Cantilever Actuator

The cantilever actuator, composed of a piece of piezoelectric material and a portion of the slider, deflects under an electric voltage V and an external vertical force F exerted on the tip as shown in Fig. 4 (a). V and F are the control voltage and air bearing force in our application. The constitutive equation of the tip deflection subject to a voltage and a force can be described as follows [18]:

$$\delta = aF + bV \tag{1}$$

$$a = \frac{1}{k_c} = \frac{4L^3}{E_p w t_p^3} \frac{\alpha\beta(1+\beta)}{\alpha^2\beta^4 + 2\alpha(2\beta + 3\beta^2 + 2\beta^3) + 1}$$

$$b = \frac{3L^2}{t_p^2} \frac{\alpha\beta(1+\beta)}{\alpha^2\beta^4 + 2\alpha(2\beta + 3\beta^2 + 2\beta^3) + 1} d_{31}$$

$$\alpha = E_s / E_p, \quad \beta = t_s / t_p$$

where the subscripts s and p stand for the slider and piezoelectric materials, respectively. E and t are the Young's modulus and beam thickness, respectively. L and w represent the length and width of the composite beam. k_c is the bending stiffness of the cantilever. d_{31} is the piezoelectric coefficient.

The deflections of the cantilever of three different slider thicknesses (0.3, 0.23, and 0.2 mm) under one volt (without external force) were calculated according to Eq. (1) and were simulated by finite element analysis (FEA) with the results as shown in Fig. 5. It was found that there exists an optimal thickness of the PZT for which the deflection is maximized for a given voltage and slider thickness.

According to Eq. (1), the cantilever is modeled as a single DOF mass-damper-spring system with (bending) stiffness k_c and damping c_c as shown in Fig. 4 (b). k_c is determined by Eq. (1) and c_c is assumed to be zero in the calculation. The equivalent mass m_{eq} is calculated by the following equation,

$$m_{eq} = \frac{k_c}{\omega_n^2} \tag{2}$$

where ω_n is the first natural frequency of the cantilever obtained by finite element analysis. ω_n is about 3380 rad/s for a pico-sized CFP slider with 300 μm thickness and 80 μm PZT plate as shown in Fig. 6. Since the bandwidth of the PZT itself is very high, the bandwidth of cantilever actuator is primarily limited by the first resonant frequency of the structure, *i.e.* about 500 kHz in this case.

2.2 2-DOF Lumped Model of the Air Bearing and Its Parameter Identification

In this section, we focus on the air bearing dynamics while the cantilever is fixed without moving relative to the rest of slider. For symmetric ABS designs and flying at 0° skew, the motion of the slider in the roll direction makes little contribution to the system response. However, the two pitch modes contribute to the slider's dynamics at the R/W transducer. This can be modeled as a 2-DOF system as shown in Fig. 7 (a). The equation of motion of this model for free vibration can be expressed in the following form,

$$[m]\{\ddot{x}\} + [c]\{\dot{x}\} + [k]\{x\} = \{0\} \tag{3}$$

where

$$\{x\} = \begin{bmatrix} z_M \\ \theta \end{bmatrix}; \; [m] = \begin{bmatrix} M & 0 \\ 0 & I_\theta \end{bmatrix};$$

$$[c] = \begin{bmatrix} c^* + c_l & -(d_t c^* - d_l c_l) \\ -(d_t c^* - d_l c_l) & d_t^2 c^* + d_l^2 c_l \end{bmatrix}$$

$$[k] = \begin{bmatrix} k^* + k_l & -(d_t k^* - d_l k_l) \\ -(d_t k^* - d_l k_l) & d_t^2 k^* + d_l^2 k_l \end{bmatrix},$$

in which z_M and θ are the displacement of the slider's mass center and the pitch angle of the slider with zero mean values, respectively. The slider's mass M and moment of inertia I_θ are 1.6×10^{-6} kg and 2.2×10^{-13} kg.m^2, respectively. The parameters that need to be identified are described as follows: k_l and k^* are the air bearing stiffness. c_l and c^* are the air bearing damping. d_l and d_t are the distance from the resultant air bearing force to the mass center of the slider. Index l or * represents the value at the leading (two pads) or trailing edge (three pads).

A linear modal analysis program developed by CML [15, 16] is used to identify the parameters. The method uses impulse responses of the slider to obtain the air bearing modal parameters, such as modal frequencies, damping ratios, mode shapes, and physical matrices (mass, stiffness, and damping). The impulse response is calculated by the constrained CML Dynamic Simulator, in which the slider's moment of inertia in the roll direction I_φ is increased to prohibit the slider from rolling and the linear disk velocity is 15 m/s. The initial impulse has to be extremely small to avoid any nonlinearity. The deflection of the cantilever is implemented in the CML Dynamic Simulator by setting the relative heights of the center trailing pad and the other four pads.

Figure 8 shows the dynamic characteristics of the CFP slider at a gap FH of 3 nm (with the cantilever actuator deflection of 24 nm). It shows the nodal lines of the two mode shapes, two modal frequencies, and two damping ratios. The frequencies and damping ratios

at several different FH's are shown in Table 1. The six parameters k^*, k_l, c^*, c_l, d_t, and d_l were determined algebraically by equating the six elements in the matrices [c] and [k] and those identified by the linear modal analysis approach. The calculated results are shown in Table 2. It is observed that only k^* and c^* exhibit significant nonlinearities. For the other four parameters, the linearized values about FH_{pt}= 2.35 nm are used in the following sections.

In the active mode of operation the cantilever actuator is expected to deflect dynamically. Hence, the center trailing pad, located at the end of the cantilever, has relative motion with respect to the other two trailing pads. A more realistic model is shown in Fig. 7 (b), where k^* and c^* are decomposed into two parts, resulting in four parameters k_t, c_t, k, and c. k_t and c_t are the air bearing stiffness and damping coefficient at the two side trailing pads of the slider body. k and c are the stiffness and damping of the center trailing pad, which is located at the end of the cantilever actuator. l (= 0.595 mm) is the distance from the slider mass center to the read/write transducer. Since the FH at the two side trailing pads is usually more than 40 nm, the linearized values of k_t and c_t are used. Table 3 shows the set of parameters for the 2-DOF model shown in Fig. 7 (b). k and c are the only nonlinear elements and c_t is set to zero for simplicity. Figures 9 (a) and (b) show plots of k and c as functions of FH at the pole tip (PT). Among the three curve fitting laws, a natural logarithm curve is found to be the best fit to the stiffness within the range of interest, giving a $k(FH_{pt})$ in units of N/m as a function of FH at the PT (FH_{pt}) in units of nm

$$k(FH_{pt}) = \beta_k \cdot \ln(FH_{pt}) + \alpha_k \tag{4}$$

The coefficients β_k and α_k for this fit are determined to be -211456 and 460671, respectively.

The damping coefficient c is almost constant for FH_{pt} between 3 and 9. A linear curve fit is applied to c for FH_{pt} less than 3 nm, giving a $c(FH_{pt})$ in units of N.sec/m as a function of FH at the PT (FH_{pt}) in units of nm

$$c(FH_{pt}) = \beta_c \cdot FH_{pt} + \alpha_c \tag{5}$$

The coefficients β_c and α_c for this fit are determined to be 0.0044 and 0.005, respectively.

This nonlinear 2-DOF model was compared to the CML Dynamic Simulator by looking at impulse responses of the slider. The results for FHpt of 2.35nm are shown in Figs. 10 and 11 in both the time and frequency (FFT) domains. H11 and H21 are the responses in the z_M and θ directions due to an impulse in the z_M direction, respectively. The results for FHpt of 3 nm are also shown in Figs. 12 and 13. In both cases, there is good agreement between the 2-DOF model and the CML Simulator.

2.3 Intermolecular Forces and Electrostatic forces

Due to the reduction in the spacing between the slider and the disk, the threshold for new nanoscale phenomena will be crossed. In particular, new forces between the slider and disk come into play, such as intermolecular and electrostatic forces. A study of the effects of intermolecular forces and electrostatic forces was presented in Gupta and Bogy [9]. The intermolecular and electrostatic forces do not have a significant effect on the flying characteristics of high flying sliders (spacings greater than 10 nm), but they become increasingly important at low spacings (below 5 nm). These forces are attractive in nature and hence result in a reduction in fly height as compared to what would be the case without them. Experimental investigations have indicated that these short range forces are one of the major instability factors in ultra low HDI.

These short range attractive forces are considered to act on the cantilever tip, *i.e.*, the 1-DOF cantilever actuator.

$$F_{act} = F_{imf} + F_{elec}$$

where

$$F_{imf} = -\frac{A'}{\left(FH_{pt}\right)^3} + \frac{B'}{\left(FH_{pt}\right)^9} \tag{6}$$

$$F_{elec} = -\frac{1}{2}\varepsilon_0 k_e A_{eq} \frac{V^2}{\left(FH_{pt}\right)^2} \tag{7}$$

and where the constants α' and β' depend on the ABS design while *A'* ($1.8\text{x}10^{-30}$) and *B'* ($2.7\text{x}10^{-88}$) are related to the material properties of the slider and disk. In this paper, the values in Thornton [19] are used. The electrostatic force due to the electrical potential across the slider and disk is shown in Eq. (7). ε_o, k_e and V are the permittivity constant ($8.85 \text{ x } 10^{-12}$ farad/m), dielectric constant of the medium (1 for air) and the potential difference between the slider and the disk. The constant A_{eq} in Eq. (7) is chosen such that the force agrees with that simulated by the CML Static Simulator. A comparison of the electrostatic forces between the CML Simulator and the model is shown in Fig. 14.

2.4 Nonlinear 3-DOF Lumped Model of CFP Sliders

Based on the analysis in the previous sections, a nonlinear 3-DOF model is constructed as shown in Fig. 15 and the equation of motion is written as follows:

$$[m]\{\ddot{x}\} + [c]\{\dot{x}\} + [k]\{x\} = \{F\} \tag{8}$$

where

$$\{x\} = \begin{bmatrix} z_M \\ \theta \\ z_m \end{bmatrix}; [m] = \begin{bmatrix} M & 0 & 0 \\ 0 & I_\theta & 0 \\ 0 & 0 & m \end{bmatrix};$$

$$[c] = \begin{bmatrix} c_t + c_l + c_c & -(d_t c_t - d_l c_l - l c_c) & -c_c \\ -(d_t c_t - d_l c_l - l c_c) & d_t^2 c_t + d_l^2 c_l + d_c^2 c_c & l c_c \\ -c_c & l c_c & c + c_c \end{bmatrix}$$

$$[k] = \begin{bmatrix} k_t + k_l + k_c & -(d_t k_t - d_l k_l - l k_c) & -k_c \\ -(d_t k_t - d_l k_l - l k_c) & d_t^2 k_t + d_l^2 k_l + d_c^2 k_c & l k_c \\ -k_c & l k_c & k + k_c \end{bmatrix}$$

$$\{F\} = \begin{bmatrix} f_{dt} + f_{dl} \\ d_l f_{dl} - d_t f_{dt} \\ F_{act} - u + f_d \end{bmatrix} = \begin{bmatrix} k_t z_{dt} + c_t \dot{z}_{dt} + k_l z_{dl} + c_l \dot{z}_{dl} \\ -d_t \left(k_t z_{dt} + c_t \dot{z}_{dt}\right) + d_l \left(k_l z_{dl} + c_l \dot{z}_{dl}\right) \\ F_{act} - u + (k z_d + c \dot{z}_d) \end{bmatrix}$$

Note that the disk profile quantities z_{dt}, z_{dl}, and z_d are assumed unknown but bounded.

Numerical simulations were conducted to calculate the responses of the system over a harmonic wavy disk. The cantilever actuator is deflected at the FH_{pt} of 2.35nm. The peak-to-peak amplitude of the waviness is assumed to be 2 nm, and three wavelengths are simulated: 1mm, 0.5mm, and 0.2mm, corresponding to frequencies of 15, 30, and 75 kHz at a linear disk velocity of 15 m/s. The FHM is obtained by subtracting z_d from z_m. Figure 16 shows the responses without including the short range forces. However, when the forces are included in the model, severe contacts were indicated and the slider could not fly stably.

3. DESIGN OF NONLINEAR COMPENSATORS

The short range forces and disk waviness cause instability of the HDI and increase the FHM. It is desirable to compensate the forces and to suppress the modulation by feedback

control. Because of the nonlinear components and uncertain disturbance in the air bearing systems, an observer-based nonlinear control or nonlinear compensator design approach is used [17]. The schematic diagram of the controller is shown in Fig. 17. Assuming that the real-time FH can be measured, we first built an observer for the state estimation and designed a sliding control law using the observer as the plant.

Equation (8) is transformed into a state-space representation as follows:

$$\begin{cases} \dot{x} = Ax + Bu + f(x) + f_d \\ y = Cx \end{cases} \tag{9}$$

The control goal is to push the FHM to zero. If z_m is used as a state, this will be a tracking problem, $z_m \rightarrow z_d$. However, the future z_d is unknown. In order to resolve this, a new state $z = z_m - z_d$ is used. The states of the system are

$$x = [x_1 \; x_2 \; x_3 \; x_4 \; x_5 \; x_6]^T = [z_M \; \dot{z}_M \; \theta \; \dot{\theta} \; z \; \dot{z}]^T$$

And

$$A = \begin{bmatrix} 0 & 1 & 0 & 0 & 0 & 0 \\ -\frac{1}{M}(k_t + k_l + k_c) & -\frac{1}{M}(c_t + c_l + c_c) & -\frac{1}{M}(-d_t k_t + d_l k_l - l k_c) & -\frac{1}{M}(-d_t c_t + d_l c_l - l c_c) & \frac{k_c}{M} & \frac{c_c}{M} \\ 0 & 0 & 0 & 1 & 0 & 0 \\ -\frac{1}{I}(-d_t k_t + d_l k_l - l k_c) & -\frac{1}{I}(-d_t c_t + d_l c_l - l c_c) & -\frac{1}{I}(d_t^2 k_t + d_l^2 k_l + l^2 k_c) & -\frac{1}{I}(d_r^2 c_r + d_f^2 c_f + l^2 c_c) & -\frac{l k_c}{I} & -\frac{l c_c}{I} \\ 0 & 0 & 0 & 0 & 0 & 1 \\ \frac{k_c}{m} & \frac{c_c}{m} & -\frac{l k_c}{m} & -\frac{l c_c}{m} & -\frac{(k + k_c)}{m} & -\frac{(c + c_c)}{m} \end{bmatrix}$$

$$B = [0 \quad 0 \quad 0 \quad 0 \quad 0 \quad -\frac{1}{m}]^T; \qquad C = [0 \quad 0 \quad 0 \quad 0 \quad 1 \quad 0]$$

$$f(x) = [0 \quad 0 \quad 0 \quad 0 \quad 0 \quad \frac{1}{m} F_{act}]^T$$

$$f_d = \begin{bmatrix} 0 \\ k_c z_d + c_c \dot{z}_d + \frac{1}{M}\left(k_t z_{dt} + c_t \dot{z}_{dt} + k_l z_{dl} + c_l \dot{z}_{dl}\right) \\ 0 \\ -lk_c z_d - lc_c \dot{z}_d + \frac{d_l}{I}\left(k_l z_{dl} + c_l \dot{z}_{dl}\right) - \frac{d_t}{I}\left(k_t z_{dt} + c_t \dot{z}_{dt}\right) \\ 0 \\ -\ddot{z}_d - \frac{1}{m}\left(k_c z_d + c_c \dot{z}_d\right) \end{bmatrix}$$

The observer is designed as

$$\dot{\hat{x}} = A\hat{x} + Bu + f(\hat{x}) + L(y - C\hat{x}) \tag{10}$$

The error dynamic is obtained by subtracting $\dot{x}$ from $\dot{\hat{x}}$

$$\dot{\tilde{x}} = \dot{\hat{x}} - \dot{x} = (A - LC)\tilde{x} - f_d \tag{11}$$

Note that ***f(.)*** and $\boldsymbol{f_d}$ represent the nonlinear components and disturbances, respectively. The observer gain matrix ***L*** is chosen as in a Luenberger observer [20] so as to place the poles of (***A-LC***) at desired locations.

The sliding surface is defined as

$$s = \dot{\hat{x}}_5 + \lambda \hat{x}_5 \tag{12}$$

We then have

$$\begin{aligned} \dot{s} &= \dot{\hat{x}}_6 + \lambda \dot{\hat{x}}_5 \\ &= \frac{1}{m}[k_c \hat{x}_1 + c_c \hat{x}_2 - lk_c \hat{x}_3 - lc_c \hat{x}_4 - (k + k_c)\hat{x}_5 - (c + c_c)\hat{x}_6 + \\ &\quad F_{act} - u] + L_6\left(x_5 - \hat{x}_5\right) + \lambda\left[\hat{x}_6 + L_5\left(x_5 - \hat{x}_5\right)\right] \end{aligned} \tag{13}$$

The control law is designed as

$$\begin{aligned} u = {} & k_c \hat{x}_1 + c_c \hat{x}_2 - lk_c \hat{x}_3 - lc_c \hat{x}_4 - (k + k_c)\hat{x}_5 - (c + c_c)\hat{x}_6 + \\ & F_{act} + m\lambda\left[\hat{x}_6 + L_5(x_5 - \hat{x}_5)\right] + mL_6(x_5 - \hat{x}_5) + m\eta s \end{aligned} \tag{14}$$

such that

$$\dot{s}s = -\eta s^2 < 0 \tag{15}$$

Eq. (15) guarantees that *s* approaches zero based on Lyapunov theory and drives the estimated FHM $\hat{x}_5$ to zero exponentially according to Eq. (12).

To investigate the controller's performance, we conducted a large number of numerical simulation experiments. Figure 18 shows the results of FHM suppression with the same conditions as used in Fig. 16. The required AC control voltages are shown in Fig. 19. It is seen that the FHM is reduced almost to zero. The effects of intermolecular and electrostatic forces (0.5V) are then included in the model. The histories of the cantilever deflection and short range attractive forces are shown in Fig. 21 and Fig. 22, respectively. Figure 20 shows that the FHM can be effectively suppressed even with an electrostatic potential of 0.5 V between the disk and slider (which is an unstable system without control). The applied control voltage is also shown in Fig. 20 (b). The observer performance is demonstrated by the comparison of the estimated and true FHM in Fig. 23 where it is seen that the error between the true and estimated values is very small.

When the electrostatic potential between the slider and disk increases from 0V to 1V (*i.e.* electrostatic forces increase), the mean control voltage shifts from 0 to about 3.3V to compensate the increased electrostatic forces, as shown in Fig. 24. This DC shift can actually decrease the applied DC control voltage required to bring the cantilever into the active operational mode.

4. CONCLUSIONS

Due to the effects of short range forces and disk morphology it is unlikely that a passive air bearing slider will be able to form a reliable head-disk interface at a spacing much less than 5 nm. Substantial research has been carried out on contact recording, in which the slider is expected to be in full contact with the disk. Several design considerations have been given in the literature, but it is still unclear how to implement such systems, namely ABS design, lubricant, and protective overcoat.

In this report, a new 3-DOF dynamic model is proposed to model a controlled flying proximity (CFP) slider, which is actuated by a layer of piezoelectric material. A linear modal analysis is used to identify the air bearing parameters. Good agreement is obtained for the air bearing dynamics between the model and the CML Dynamic Simulator. An observer-based nonlinear sliding mode controller is designed based on the model. Numerical studies show that a FH below 3 nm is achieved and the FHM due to disk waviness is effectively reduced in the presence of short range attractive forces.

ACKNOWLEDGEMENTS

This study is supported by the Computer Mechanics Laboratory (CML) at the University of California, Berkeley. J. Y. Juang has also been supported by The California State Nanotechnology Fellowship.

REFERENCES

1. Yanagisawa, M., Sato, A., Ajiki, K., and Watanabe, F., 1997, "Design Concept of Contact Slider for High-Density Recording," *Electronics and Communications in Japan*, part 2, vol.80, pp.43-48
2. Ono K., Iida K., and Takahashi K., 1999, "Effects of Design Parameters on Bouncing Vibrations of a Single-DOF Contact Slider and Necessary Design Conditions for Perfect Contact Sliding," *Journal of Tribology*, vol.121, no.3, pp.596-603
3. Ono, K. and Takahashi, K., 1999, "Analysis of Bouncing Vibrations of a 2-DOF Tripad Contact Slider Model With Air Bearing Pads Over a Harmonic Wavy Disk Surface," *Journal of Tribology*, vol. 121, pp. 939-947
4. Iida, K. and Ono, K., 2001, "Analysis of Bouncing Vibrations of a 2-DOF Model of Tripad Contact Slider Over a Random Wavy Disk Surface," *Journal of Tribology*, vol. 123, pp. 159-167
5. Iida, K., Ono, K., and Yamane, M., 2002, "Dynamic Characteristics and Design Consideration of a Tripad Slider in the Near-Contact Regime," *Journal of Tribology*, vol.124, pp.600-606
6. Ono K. and Iida K., 2000, "Statistical Analysis of Perfect Contact and Wear Durability Conditions of a Single-DOF Contact Slider," *Journal of Tribology*, vol.122, no.1, pp.238-245
7. Iida, K. and Ono, K., 2003, "Design Consideration of Contact/ Near-Contact Sliders Based on a Rough Surface Contact Model," *Journal of Tribology*, vol.125, no.3, pp.562-570

8. Yamane, M., Ono, K., and Yamaura, H., 2003, "2-DOF Analysis of Friction-Induced Slider Vibrations in a Near-Contact Regime," *Proceedings of STLE/ASME Int. Joint Tribology Conf.*, Oct., 26-29 2003. TRIB-0046
9. Gupta, V. and Bogy, D.B., "Dynamics of Sub-5nm Air Bearing Sliders in the Presence of Electrostatic and Intermolecular Forces at the Head Disk Interface," *IEEE Transactions on Magnetics* (accepted for publication)
10. Kurita, M. and Suzuki, K., 2004, "Flying-Height Adjustment Technologies of Magnetic Head Sliders," *IEEE Transactions on Magnetics*, vol. 40, no. 1, pp. 332-336.
11. Kurita, M., Tsuchiyama, R., Tokuyama, M., Xu, J., Yoshimura, Y., Kohira, H., Su, L. Z., and Kato, K., 2003, "Flying-Height Adjustment of a Magnetic Head Slider with a Piezoelectric Micro-Actuator," *Intermag Conf., Boston, MA*, pp. GP-06.
12. Tagawa, N., Kitamura, K., and Mori, A., 2003, "Design and Fabrication of MEMS-Based Active Sliders Using Double-Layered Composite PZT Thin Films in Hard Disk Drives," *IEEE Transactions on Magnetics*, vol. 39, no. 39, pp. 926-931.
13. Li, Amei, Liu, Xinqun, Clegg, W., Jenkins, D. F. L., and Donnelly, T., 2003, "Real-Time Method to Measure Head Disk Spacing Variation Under Vibration Conditions," *IEEE Trans. Instru. And Measur.*, vol. 52, no. 3, pp. 916-920.
14. Liu, Xinqun, Li, Amei, Clegg, W., Jenkins, D. F. L., and Davey, P., 2002, "Head-Disk Spacing Variation Suppression via Active Flying Height Control," *IEEE Trans. Instru. And Measur.*, vol. 51, no. 5, pp. 897-901.
15. Zeng, Q. H., Chen, L. S., and Bogy, D. B., 1996, "A Modal Analysis Method for Slider-Air Bearings in Hard Disk Drives," Technical Report No. 96-021, Computer Mechanics Lab., Dept. of Mechanical Engineering, University of California at Berkeley.

16. Zeng, Q. H. and Bogy, D. B., 1997, " The CML Slider-Air Bearing Parameter Identification Program," Technical Report No. 97-006, Computer Mechanics Lab., Dept. of Mechanical Engineering, University of California at Berkeley
17. Song, B. and Hedrick, J. K., 2003, "Observer-Based Dynamic Surface Control for Lipschitz Nonlinear Systems," *42nd IEEE International Conference on Decision and Control, Piscataway, NJ, USA*, pp. 874-9.
18. Smits, J. G. and Choi, W.-S., 1991, "The Constituent Equations of Piezoelectric Heterogeneous Bimorphs," *IEEE Trans. Ultrason., Ferroelect., Freq. Contr.*, vol. 38, no. 3, pp. 256-270.
19. Thornton, B. H. and Bogy, D. B., 2004, "A Parametric Study of Head-Disk Interface Instability Due to Intermolecular Forces," *IEEE Transactions on Magnetics*, vol. 40, no. 1, pp. 337-344.
20. Ogata, K., 1967, "State Space Analysis of Control Systems," Englewood Cliffs, N.J., Prentice-Hall.

FH_{pt} (nm)	Deflection (nm)	pitch (μrad)	Frequency 1 (kHz)	Frequency 2 (kHz)	Damping ratio 1 (%)	Damping ratio 2 (%)
0.41	35	209.52	70	232	4.7817	0.4452
0.70	33	212.32	70	217	4.7304	0.6563
2.35	26	221.19	69	175	4.8100	1.4600
3.07	24	223.34	69	165	4.8500	1.7500
20.22	0	235.10	68	112	5.2300	2.6800

Table 1. The results of parameter identification of 2-DOF air bearing at five flying heights.

FH_{pt} (nm)	Deflection (nm)	k^* (MN/m)	k_l (MN/m)	c_* (N.sec/m)	c_l (N.sec/m)	d_l (mm)	d_t (mm)
0.41	35	1.080	0.214400	0.00648	0.0462	0.2418	0.5440
0.70	33	0.960	0.203172	0.0075	0.0443	0.2650	0.5415
2.35	26	0.625	0.194725	0.01554	0.04386	0.2717	0.5358
3.07	24	0.590	0.182977	0.01767	0.0393	0.2966	0.5126
20.22	0	0.310	0.180145	0.025	0.055	0.2872	0.4610

Table 2. The results of parameter identification of 2-DOF air bearing at five flying heights.

FH_{pt} (nm)	Deflection (nm)	k (MN/m)	c (N.sec/m)	k_t (MN/m)	k_l (MN/m)	c_l (N.sec/m)	d_l (mm)	d_t (mm)
0.41	35	0.69	0.00650	0.3	0.194725	0.04386	0.2717	0.5358
1.75	28	0.35	0.01300	0.3	0.194725	0.04386	0.2717	0.5358
2.35	26	0.28	0.01554	0.3	0.194725	0.04386	0.2717	0.5358
3.07	24	0.225	0.01800	0.3	0.194725	0.04386	0.2717	0.5358
5.75	18.5	0.105	0.01900	0.3	0.194725	0.04386	0.2717	0.5358
9.02	13.5	0.04	0.01900	0.3	0.194725	0.04386	0.2717	0.5358

Table 3. The identified k and c1 at several flying heights with other parameters as in the case of 2.35 nm. The value of c is set to be zero.

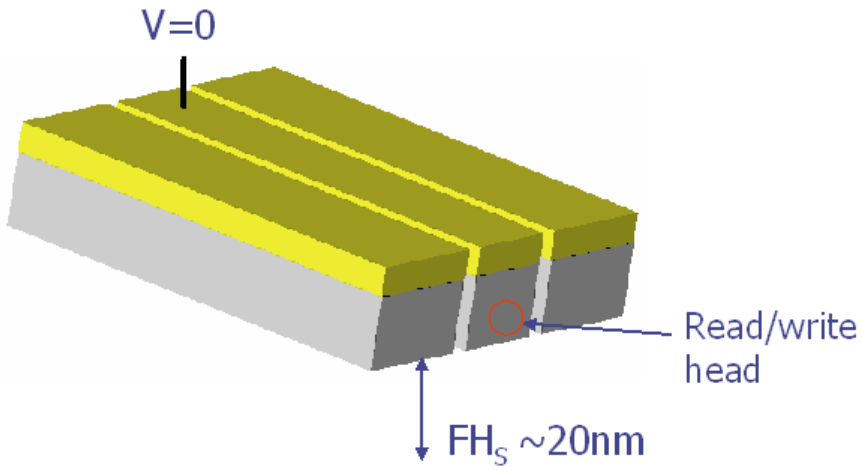

(a) Passive mode (no control algorithm is applied)

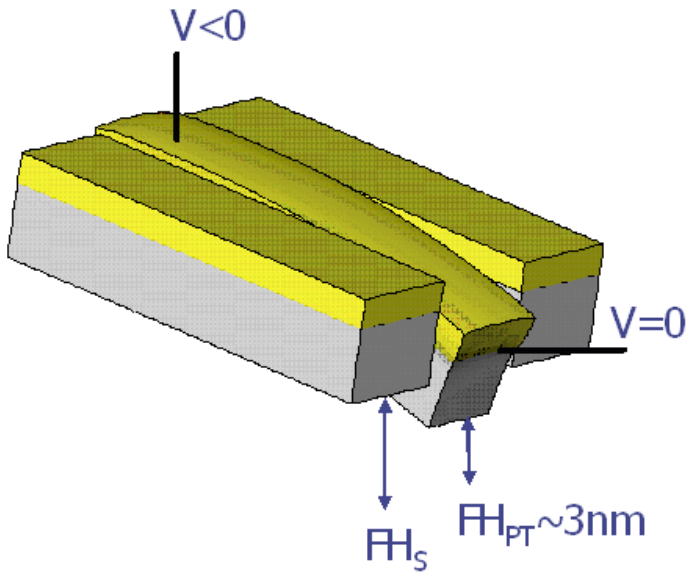

(b) Active mode (control algorithm is applied)

Fig. 1. Two operational modes of a controlled flying proximity slider with PZT actuation. The R/W transducer is not shown in this diagram.

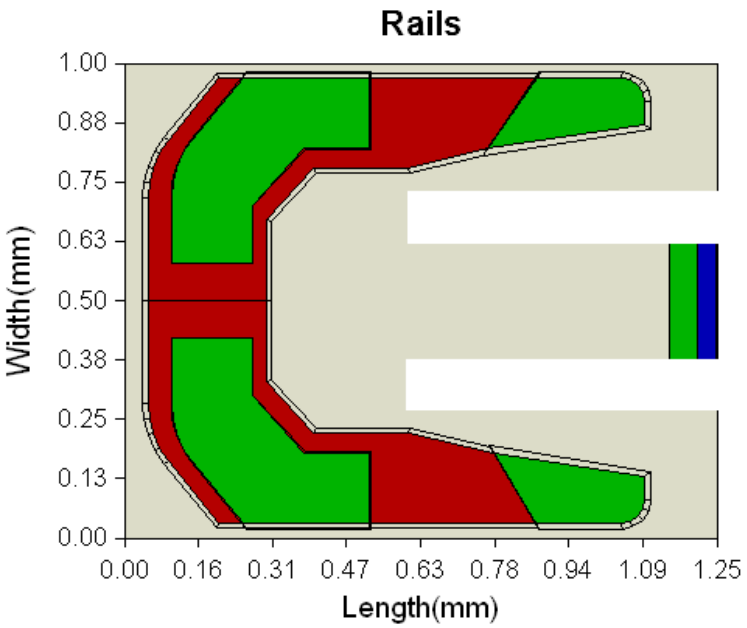

Fig. 2 An ABS design of CFP sliders

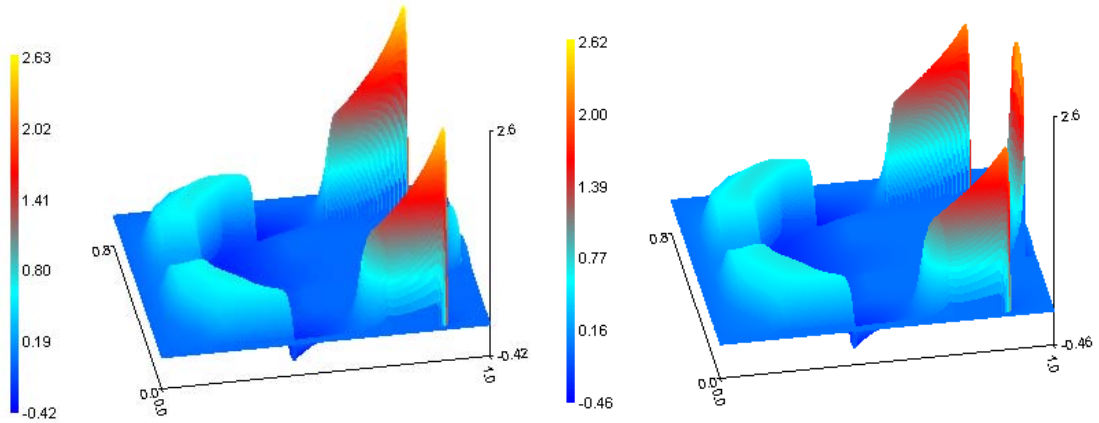

(a) (b)

Fig. 3. Air pressure distributions of the ABS in Fig. 2. (a) passive mode and (b) active mode. The gap flying height has been reduced from 20 nm to 2.35 nm.

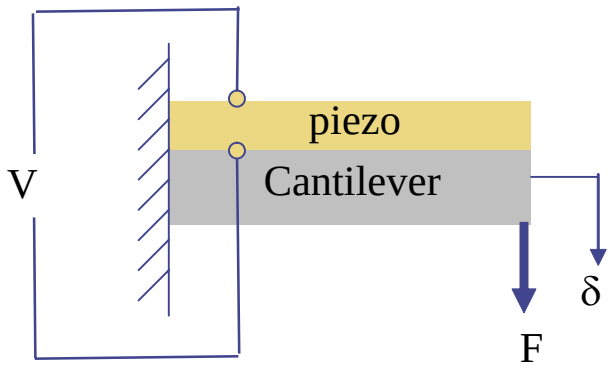

(a)

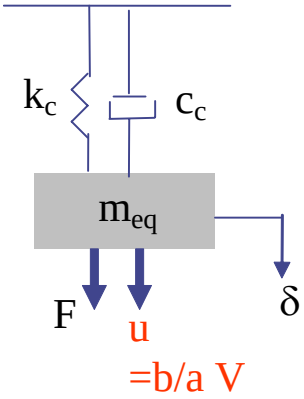

(b)

Fig. 4. Schematic diagram of a piezoelectric composite beam actuator (a) and the 1-DOF model.

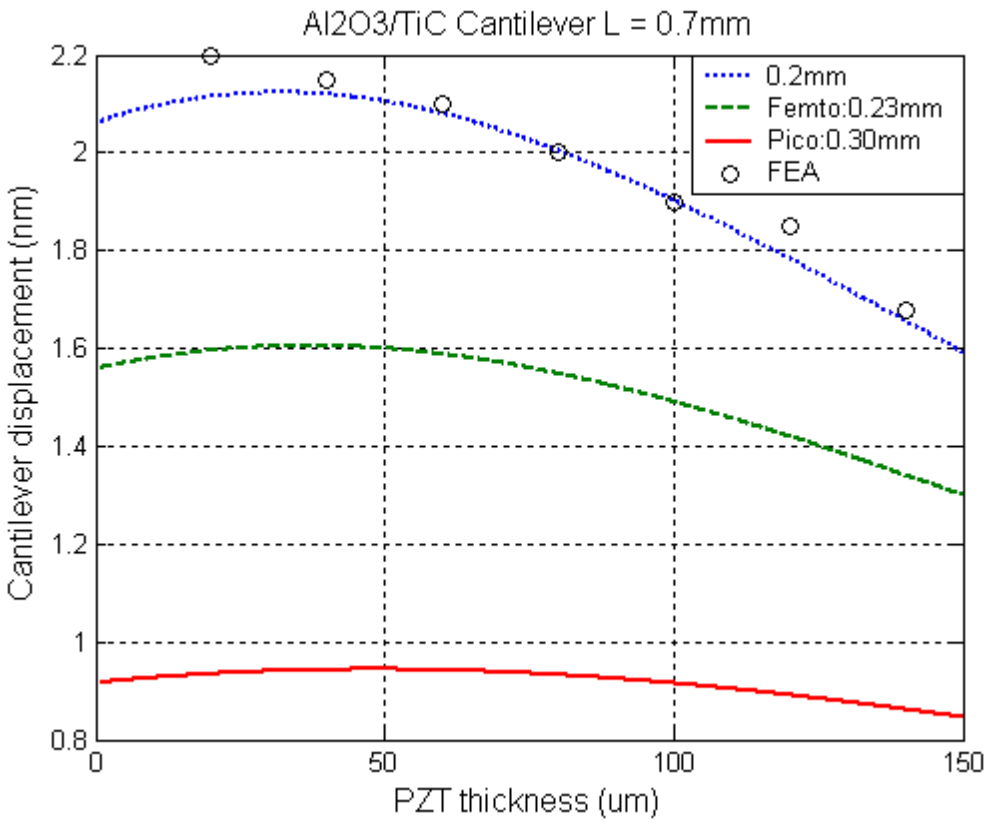

Fig. 5. The deflection of the cantilever tip under 1V. The solid line is for a pico-slider thickness, the dash line is for the femto slider thickness. FEA shows the results carried out by finite element analysis. E_p=62GPa, E_c=398GPa, d_{31}=-360x10^{-12}m/V.

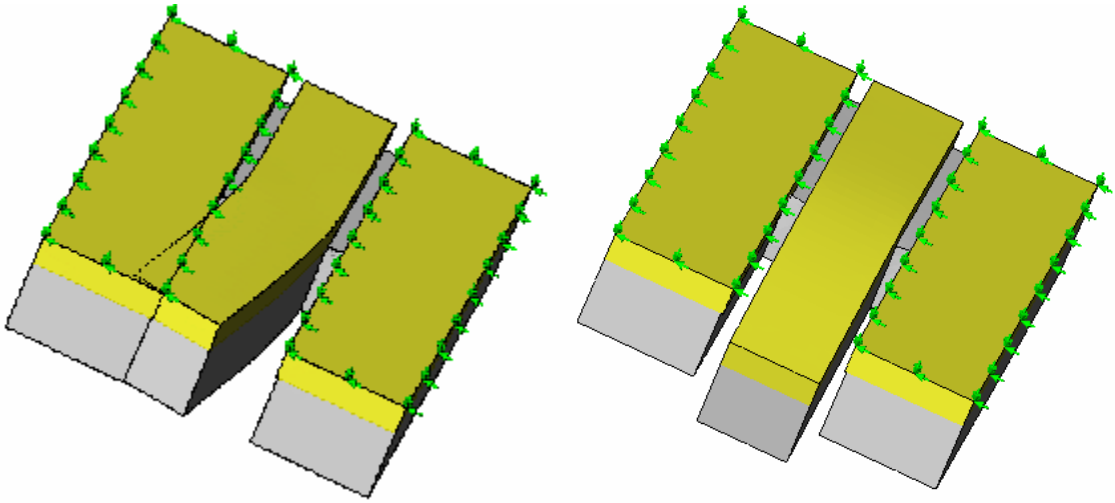

(a) the first mode (in-plane) (b) the second mode (out-of-plane)

Fig. 6. The first two modes of a pico-sized CFP slider simulated by finite element analysis (COSMOSDesignSTAR®). The natural frequencies are 538 and 550 kHz. (Slider thickness=300 μm, PZT thickness=80 μm).

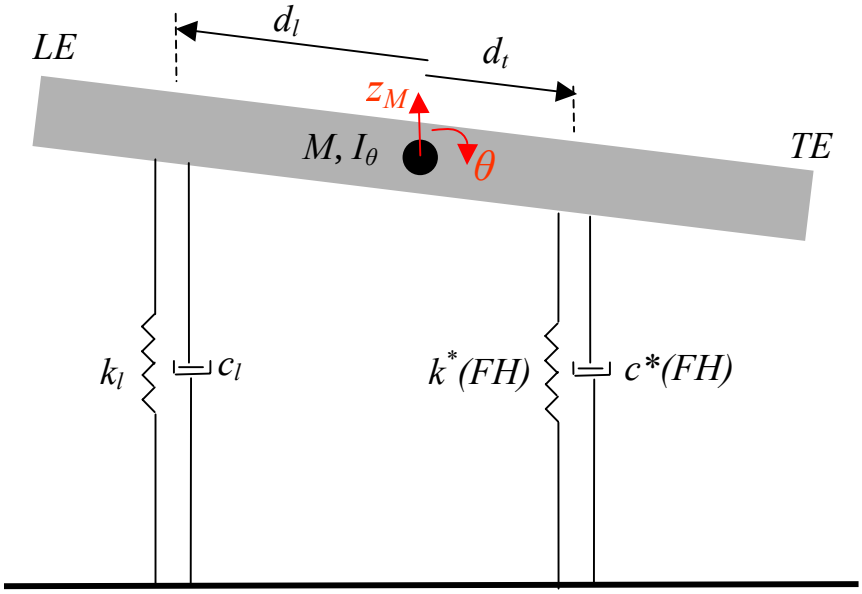

(a)

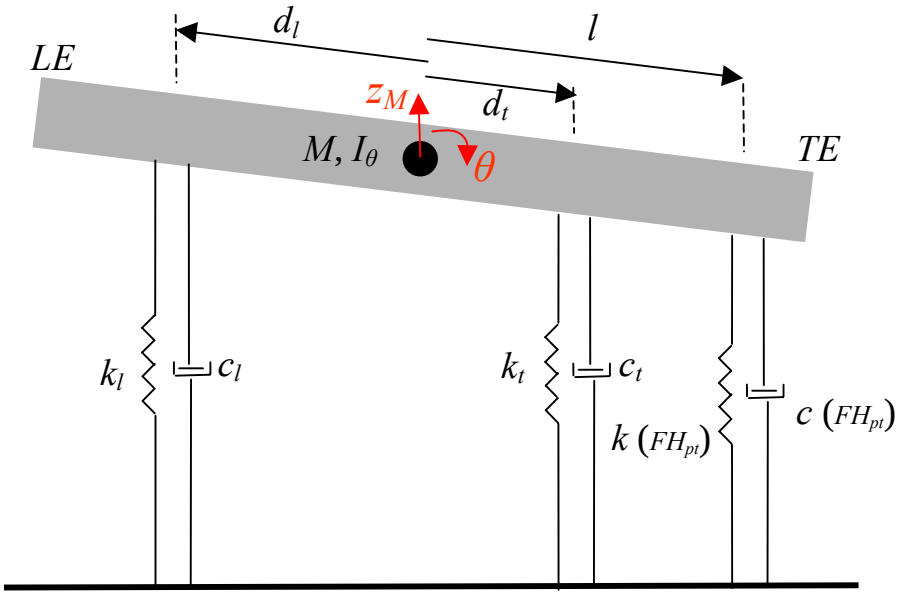

(b)

Fig. 7. Schematic diagram of 2-DOF dynamic model of CFP sliders. The cantilever is fixed such that there is no relative motion between the slider and the cantilever.

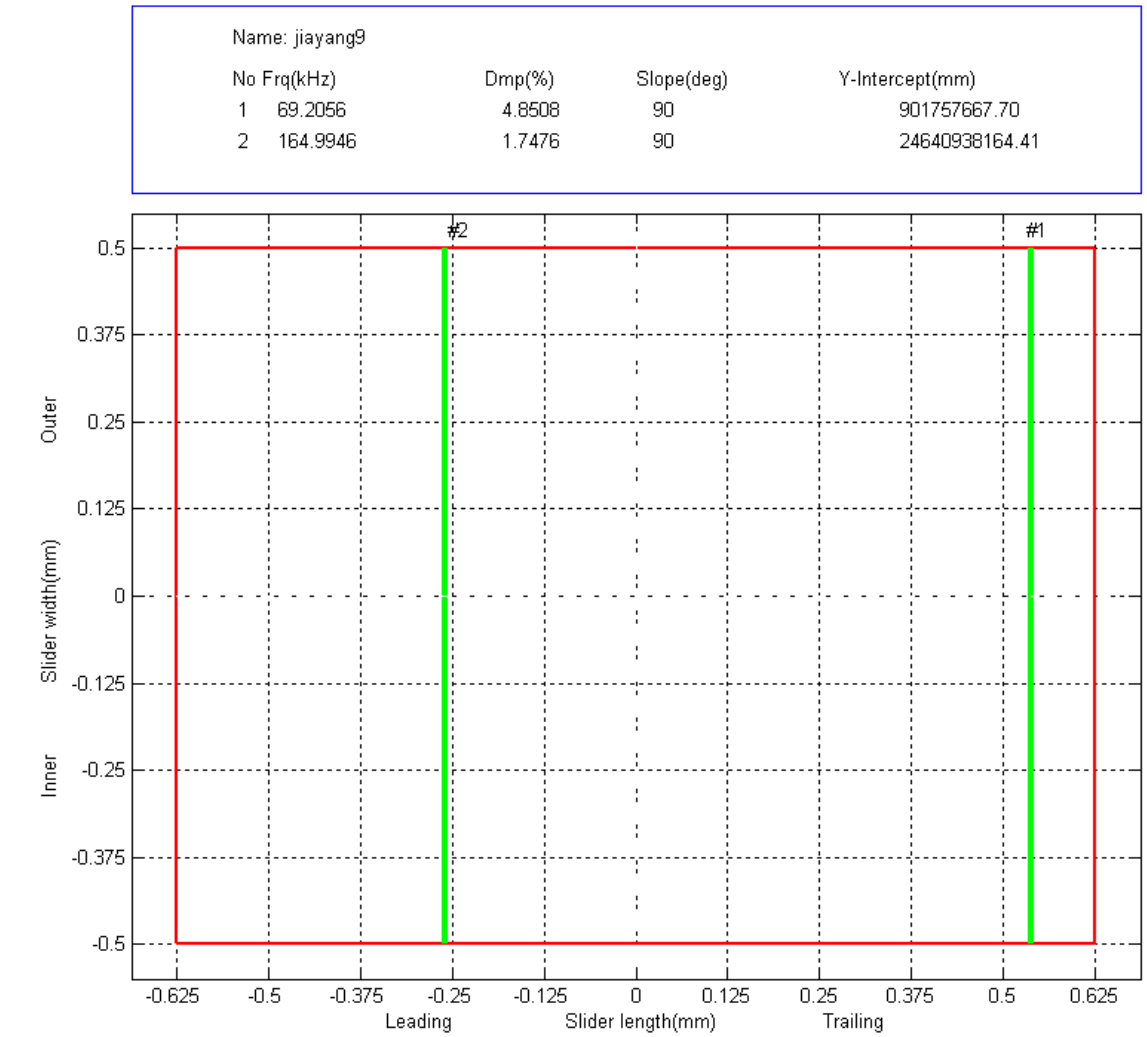

Fig. 8. Dynamic characteristics of the CFP slider at FHpt = 3.07 nm.

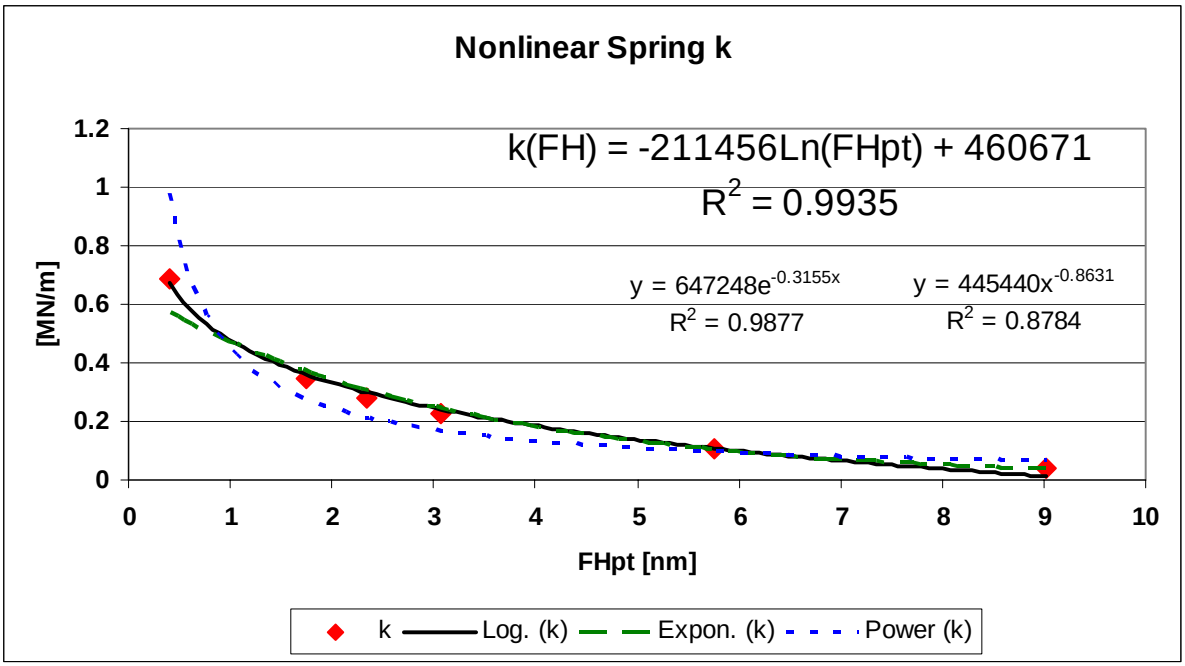

(a)

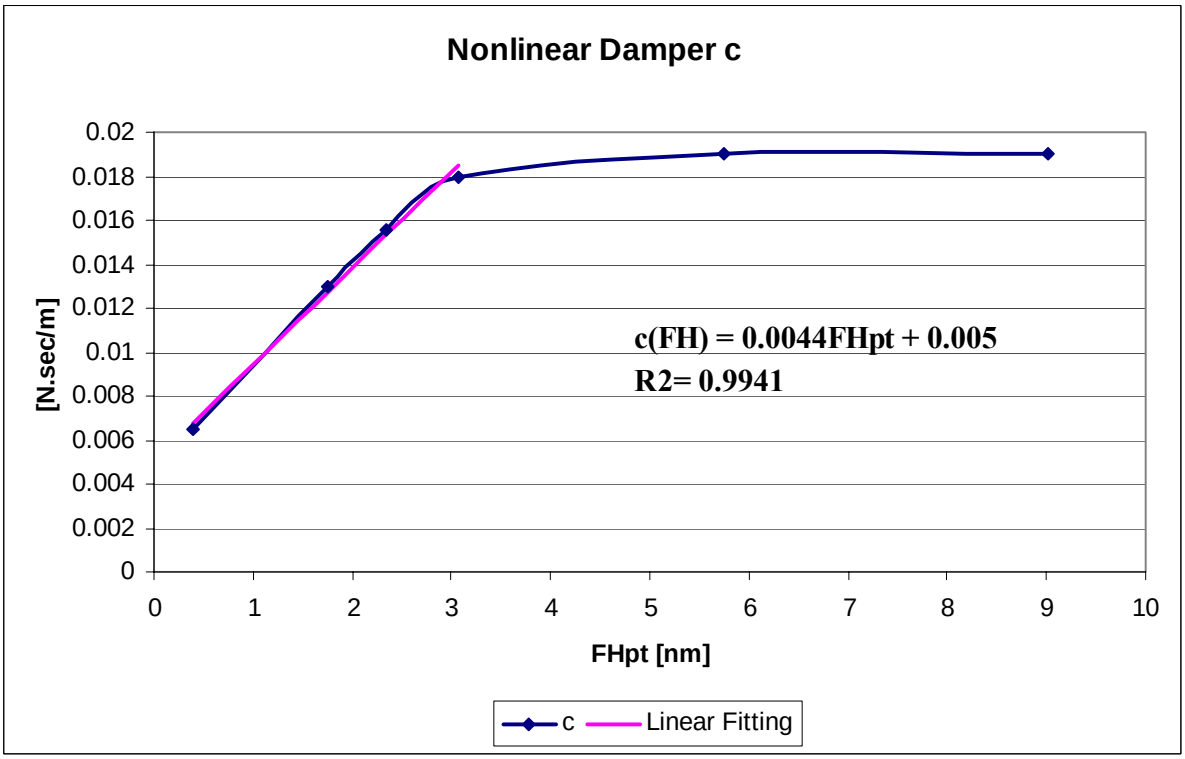

(b)

Fig. 9. (a) Nonlinear stiffness k and (b) nonlinear damping c1 as a function of FH at the PT.

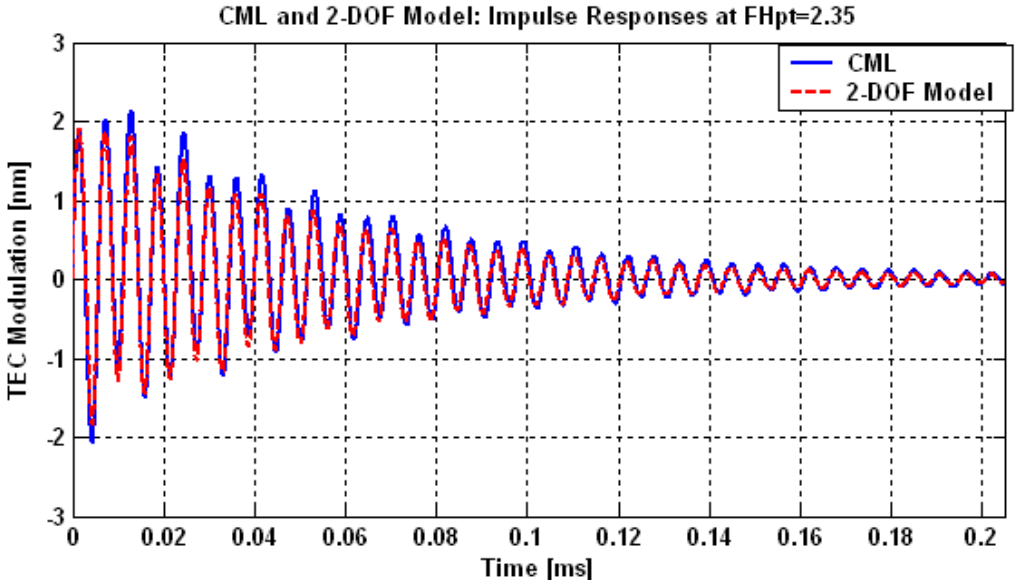

(a)

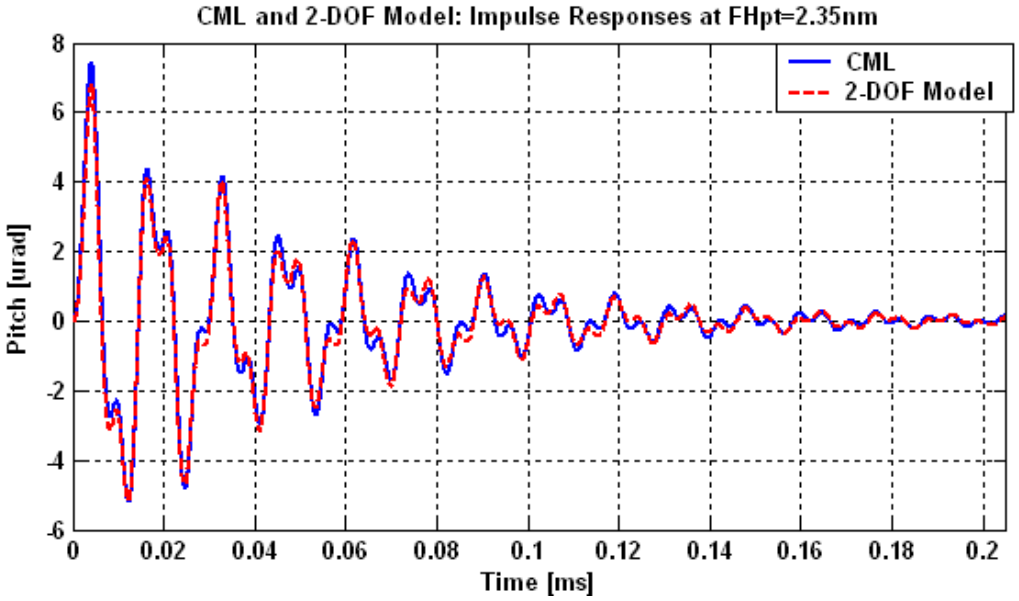

(b)

Fig. 10. Impulse responses (initial velocity 0.002 m/s in z direction) of CFP slider simulated by the 2-DOF model and the CML Dynamic Simulator: (a) TEC FH modulation and (b) pitch modulation about the equilibrium of FH_{pt} = 2.35nm

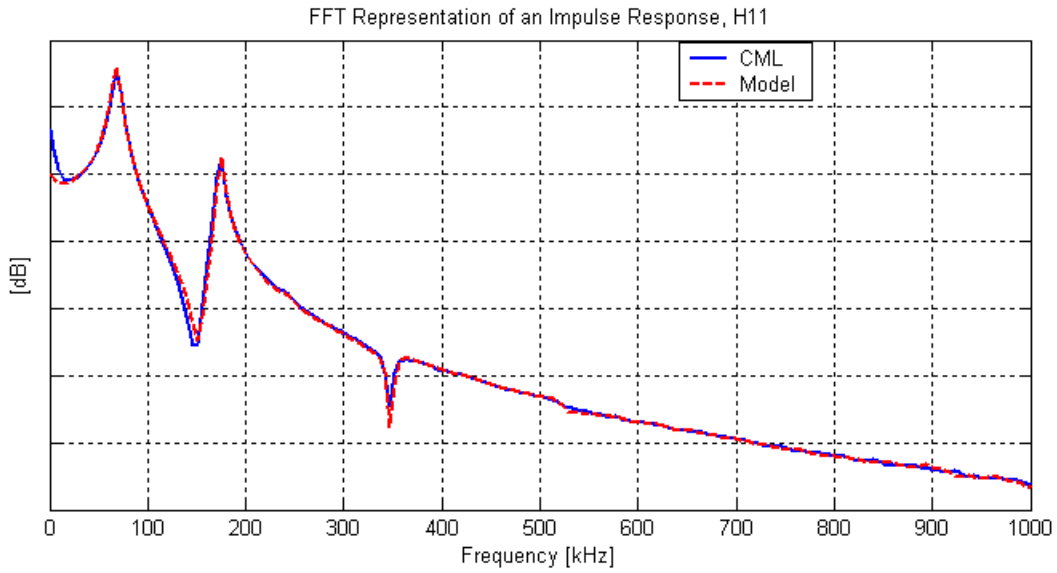

(a)

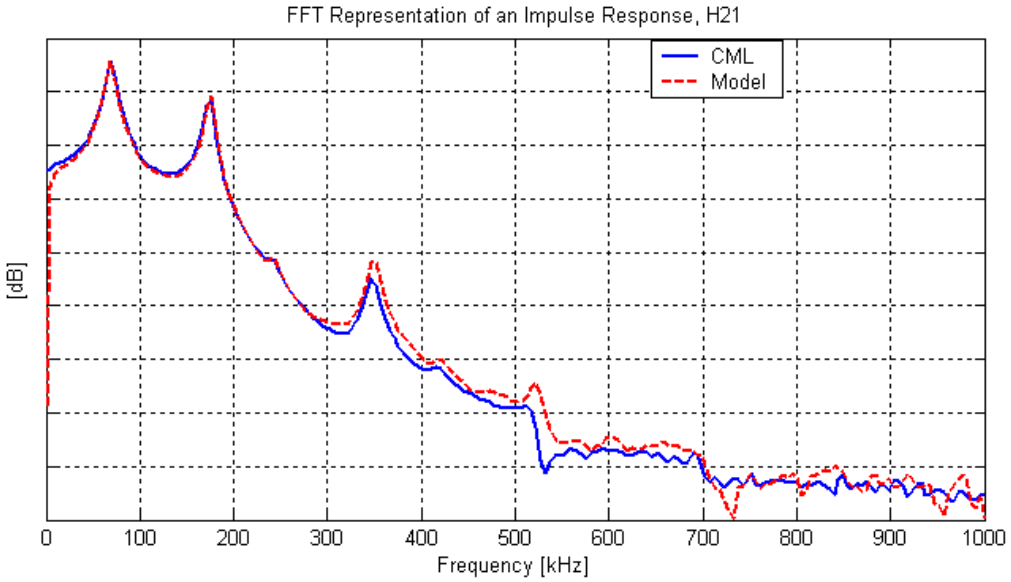

(b)

Fig. 11. Impulse responses (initial velocity 0.002 m/s in z direction) of CFP slider simulated by the 2-DOF model and the CML Dynamic Simulator shown in the frequency (FFT) domains: (a) the response of TEC FH and (b) the response of pitch about the equilibrium of FHpt = 2.35nm

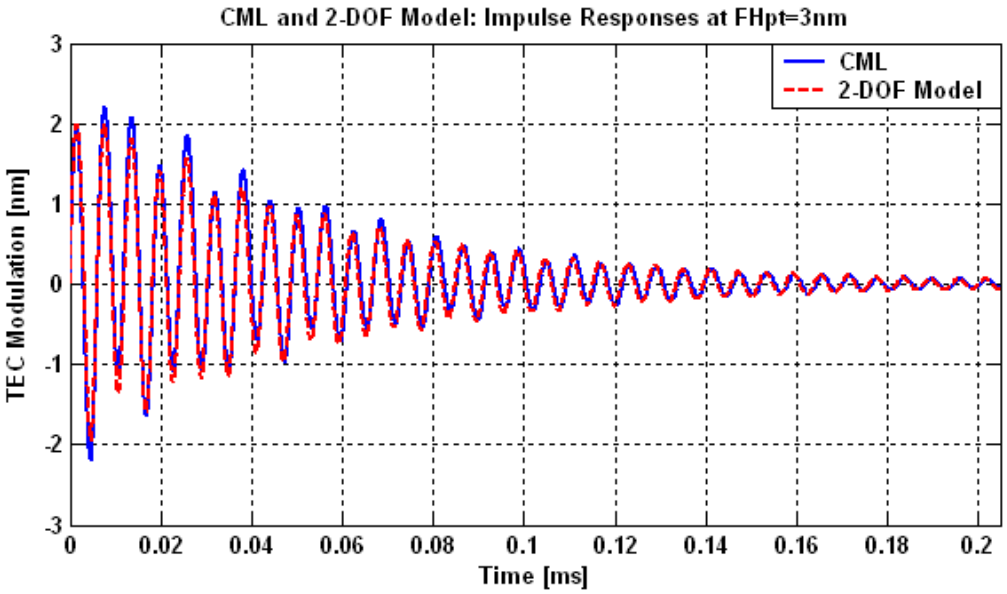

(a)

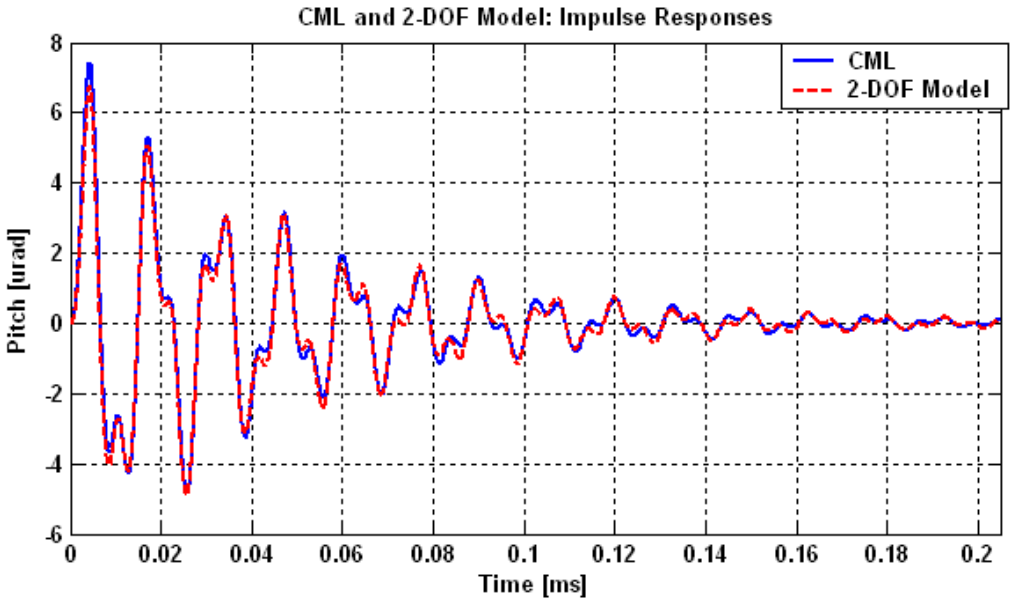

(b)

Fig. 12. Impulse responses (initial velocity 0.002 m/s in z direction) of CFP slider simulated by the 2-DOF model and the CML Dynamic Simulator: (a) TEC FH modulation and (b) pitch modulation about the equilibrium of FH_{pt} = 3.07nm

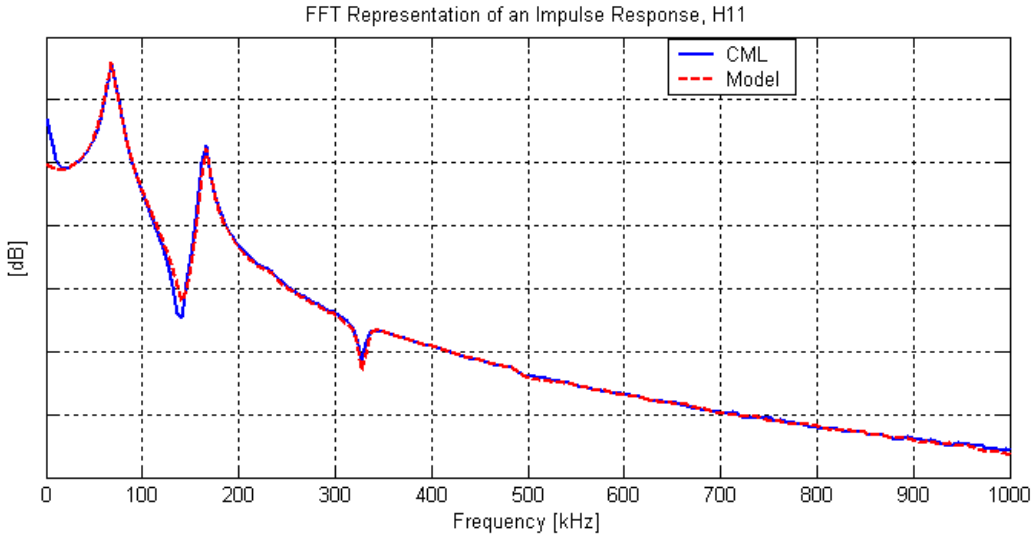

(a)

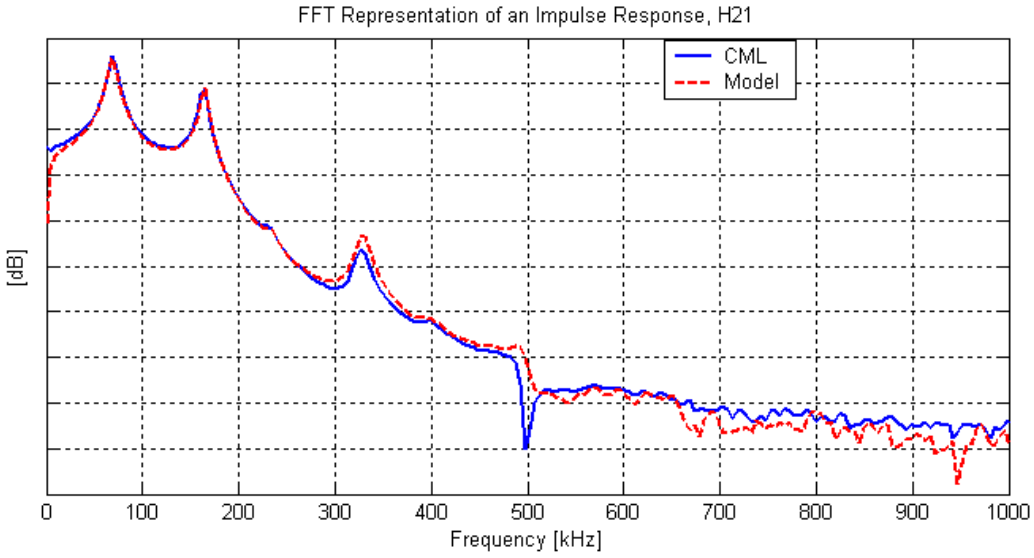

(b)

Fig. 13. Impulse responses (initial velocity 0.002 m/s in z direction) of CFP slider simulated by the 2-DOF model and the CML Dynamic Simulator shown in the frequency (FFT) domains: (a) the response of TEC FH and (b) the response of pitch about the equilibrium of FHpt = 3.07nm

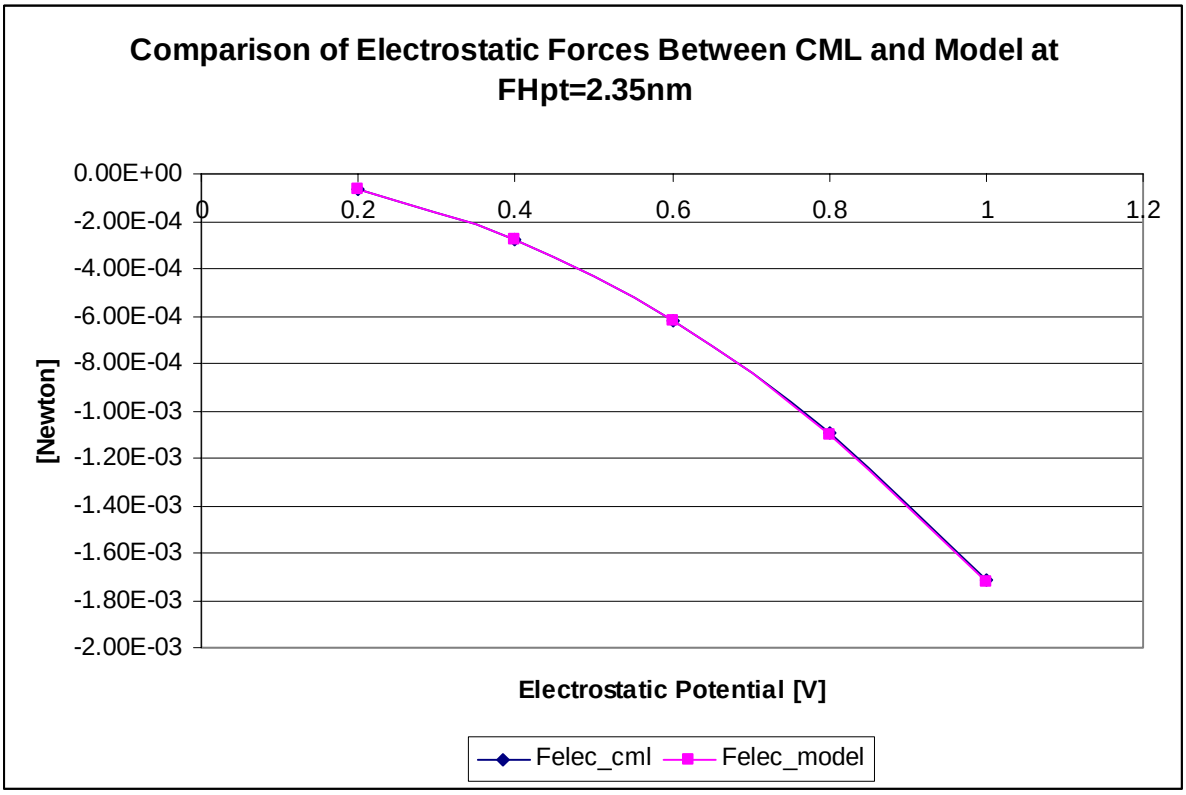

Fig.14 . Comparison of electrostatic forces between CML Simulator and model. The forces are calculated when the slider is fixed at FHpt = 2.35 nm and pitch = 221 μrad.

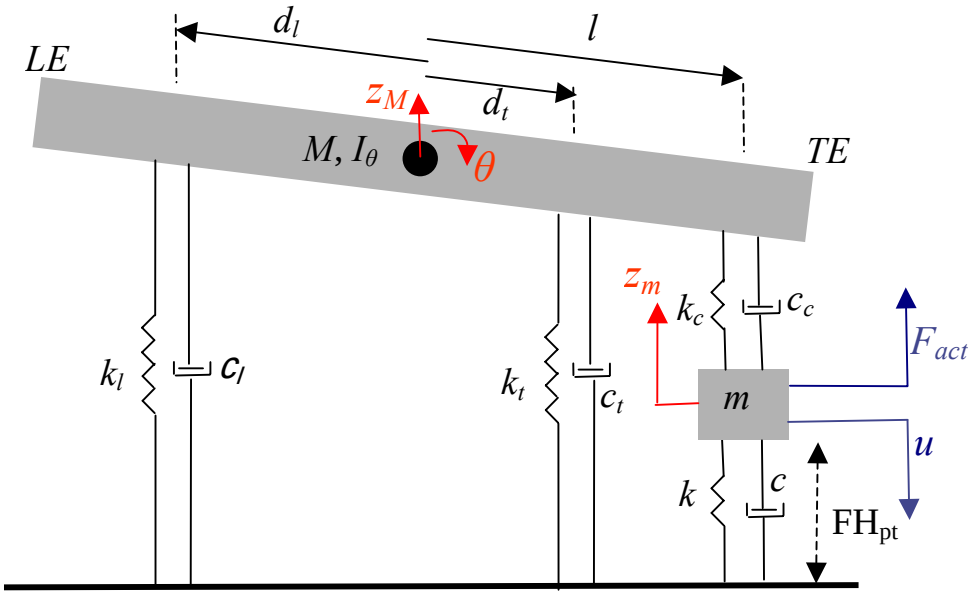

Fig. 15. Schematic diagram of 3-DOF dynamic model of CFP sliders.

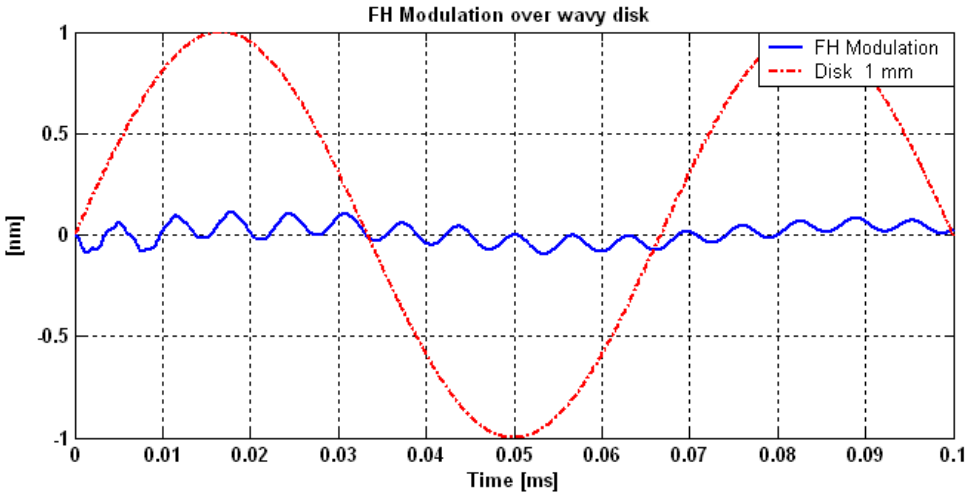

(a) The wavelength of disk waviness: 1 mm

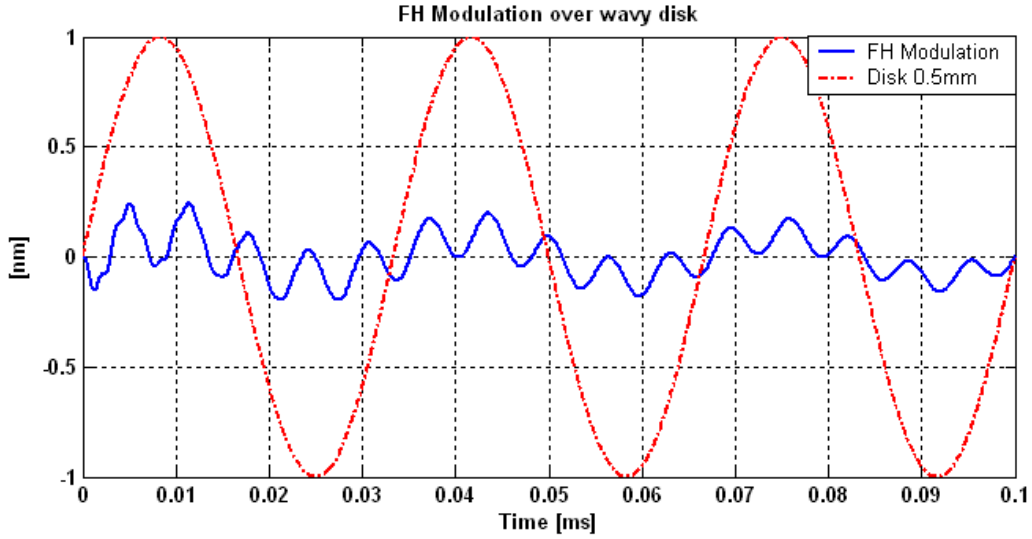

(b) The wavelength of disk waviness: 0.5 mm

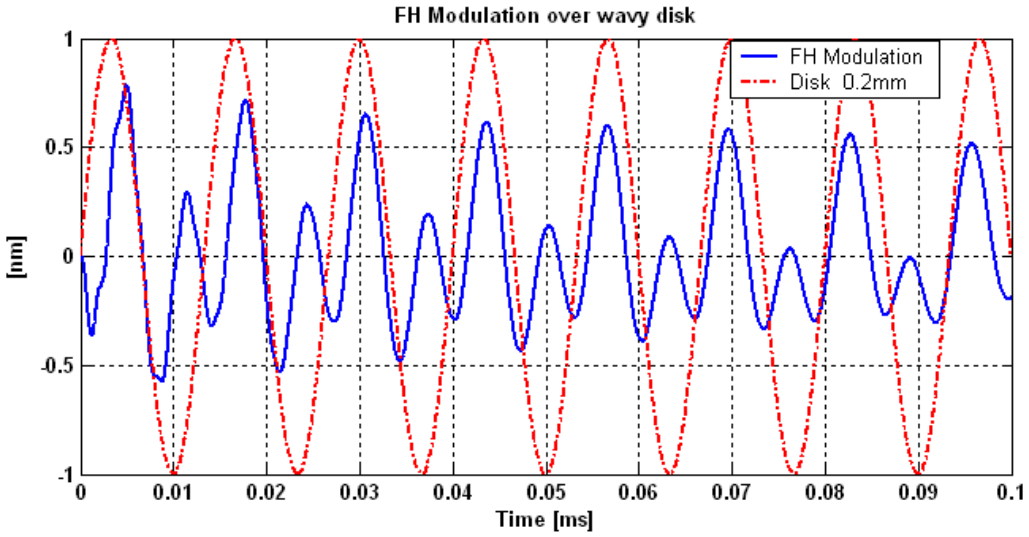

(c) The wavelength of disk waviness: 0.2 mm

Fig. 16. FHM of 3-DOF over three disk wavelengths without short range forces.

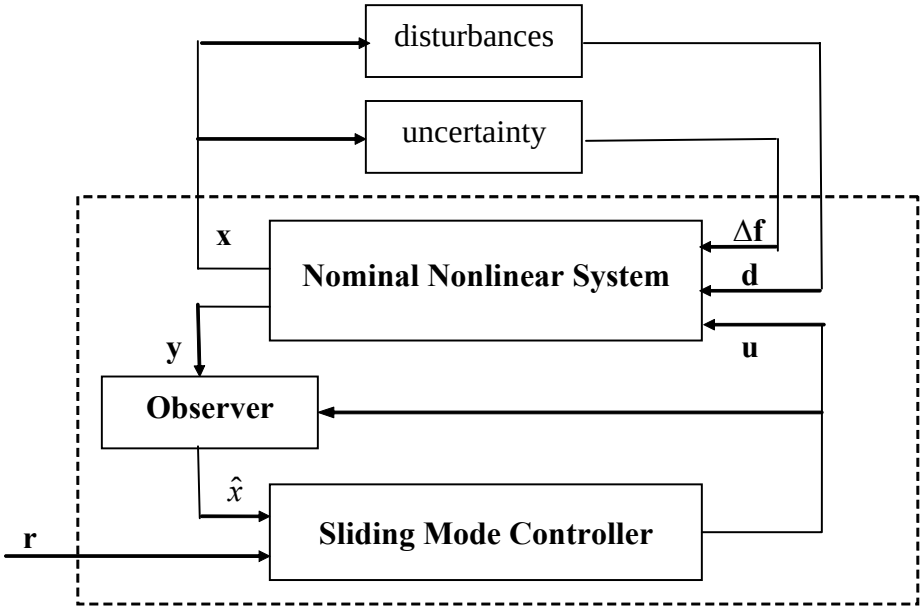

Fig. 17. Schematic framework of observer-based sliding mode controller

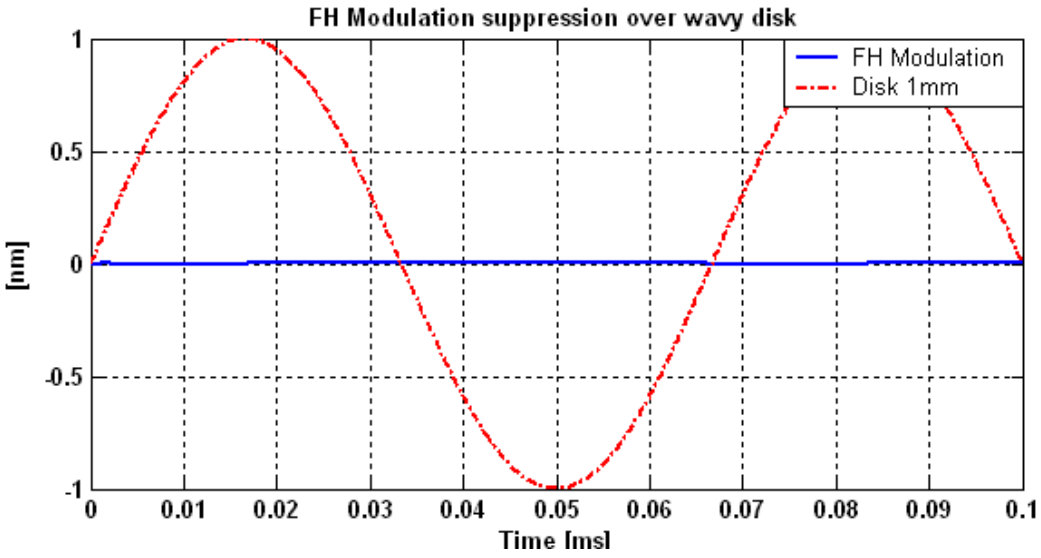

(a) The wavelength of disk waviness : 1 mm

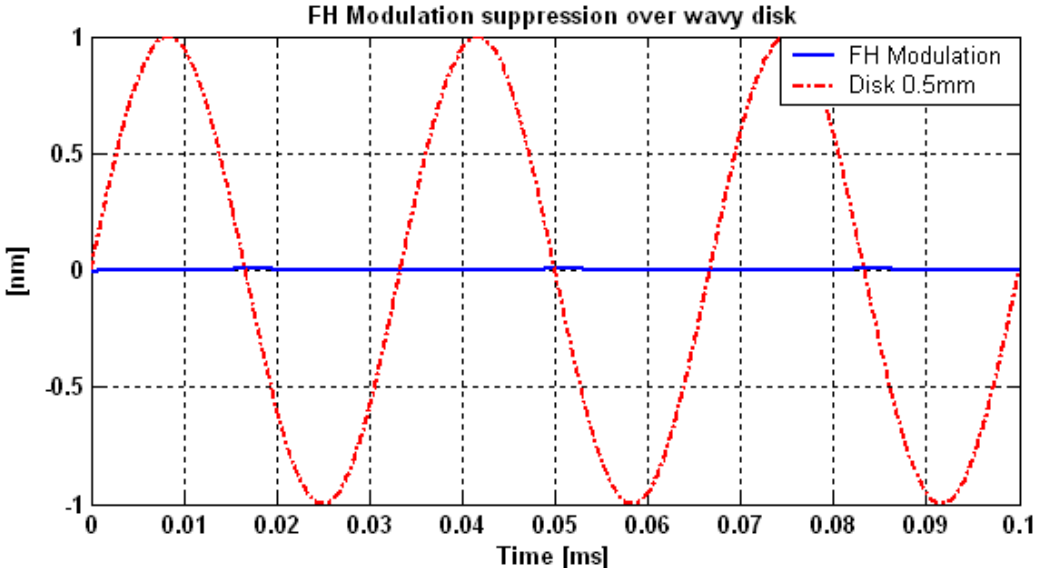

(b) The wavelength of disk waviness: 0.5 mm

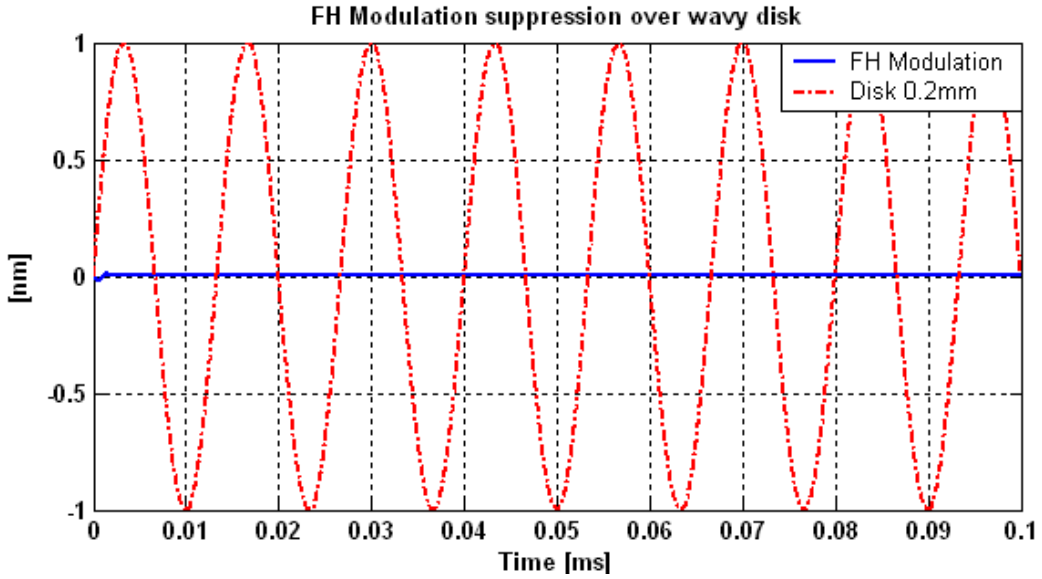

(c) The wavelength of disk waviness: 0.2 mm

Fig. 18. The results of FHM suppression of the CFP slider. Simulations conditions are the same as those in Fig. (16).

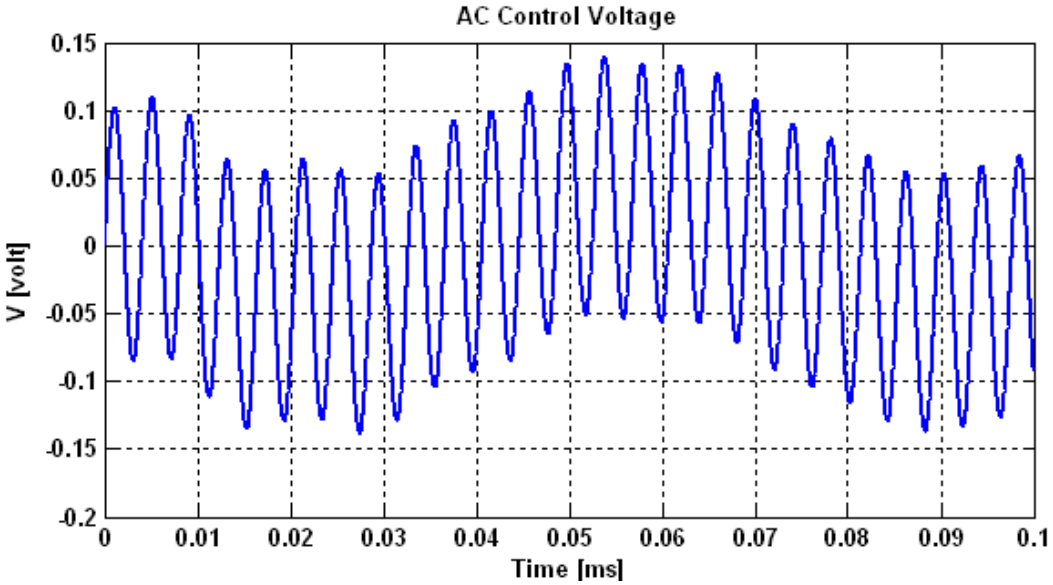

(a)

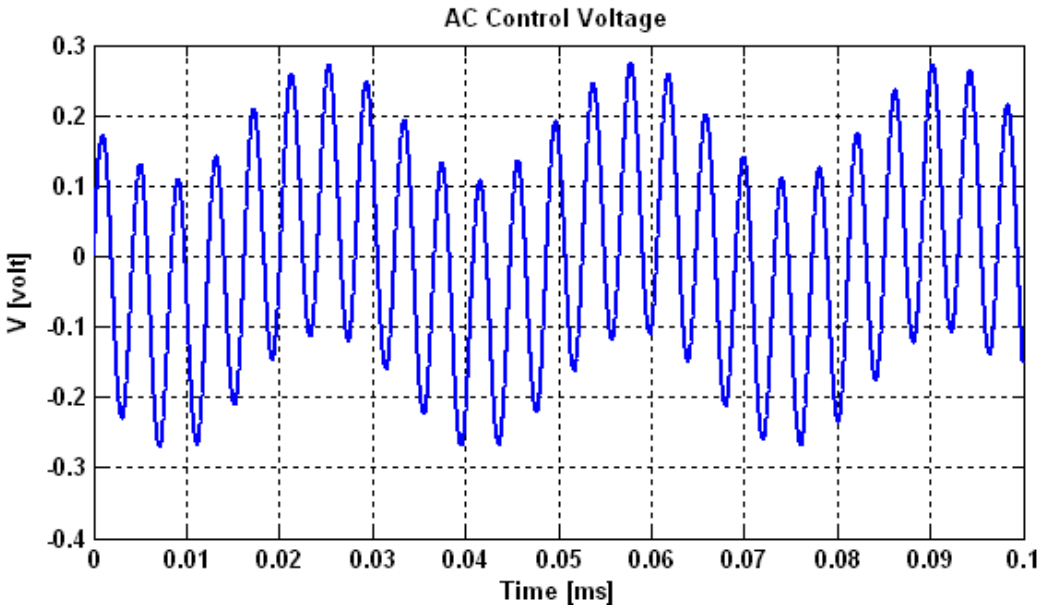

(b)

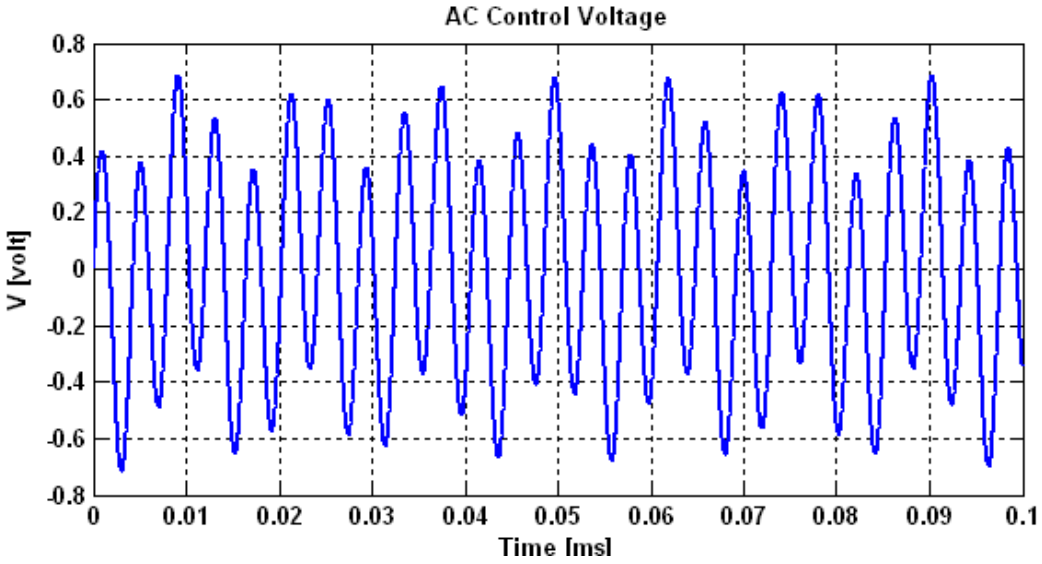

(c)

Fig. 19. The voltage determined by the control law for cases in Fig. (18)

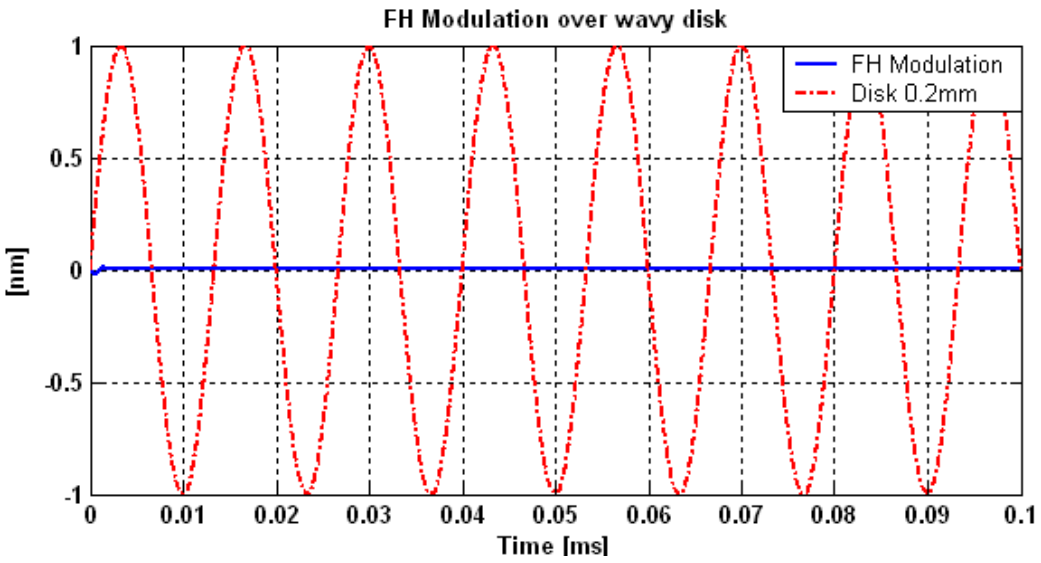

(a)

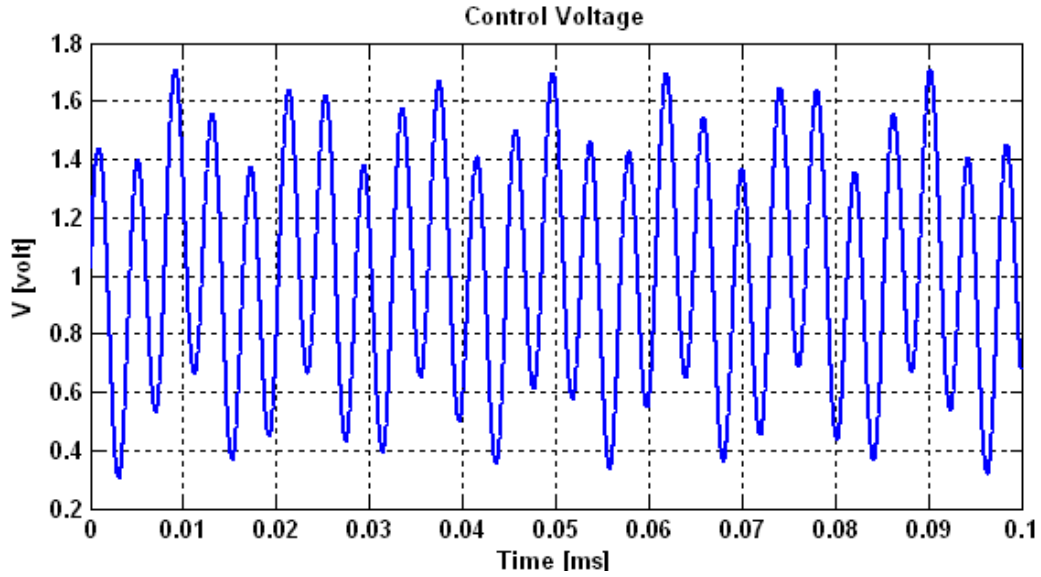

(b)

Fig. 20. (a) The results of FHM suppression of the CFP slider in the presence of intermolecular and electrostatic forces (0.5 V). The disk waviness wavelength is 0.2 mm. (b) the control voltage.

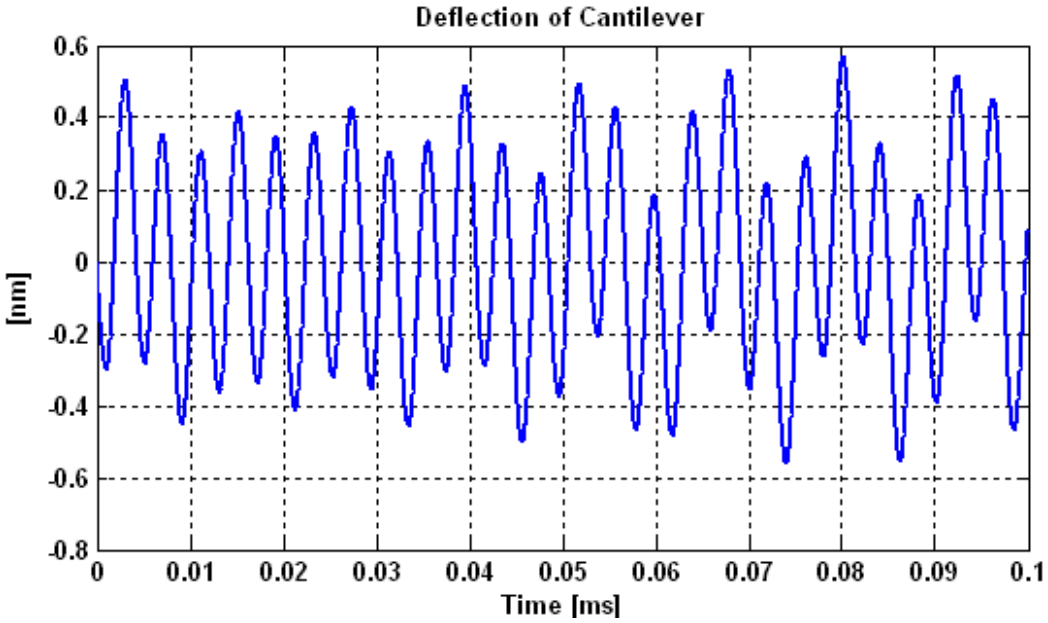

Fig. 21. Deflection of the cantilever actuator.

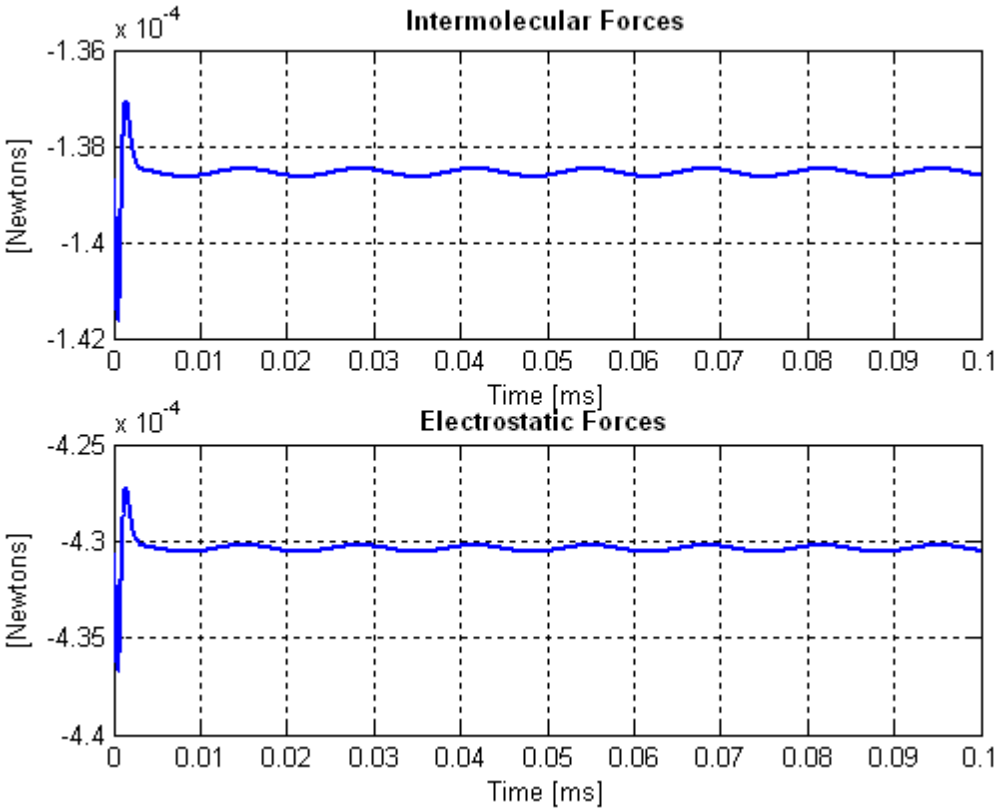

Fig. 22. The intermolecular and electrostatic forces (0.5V)

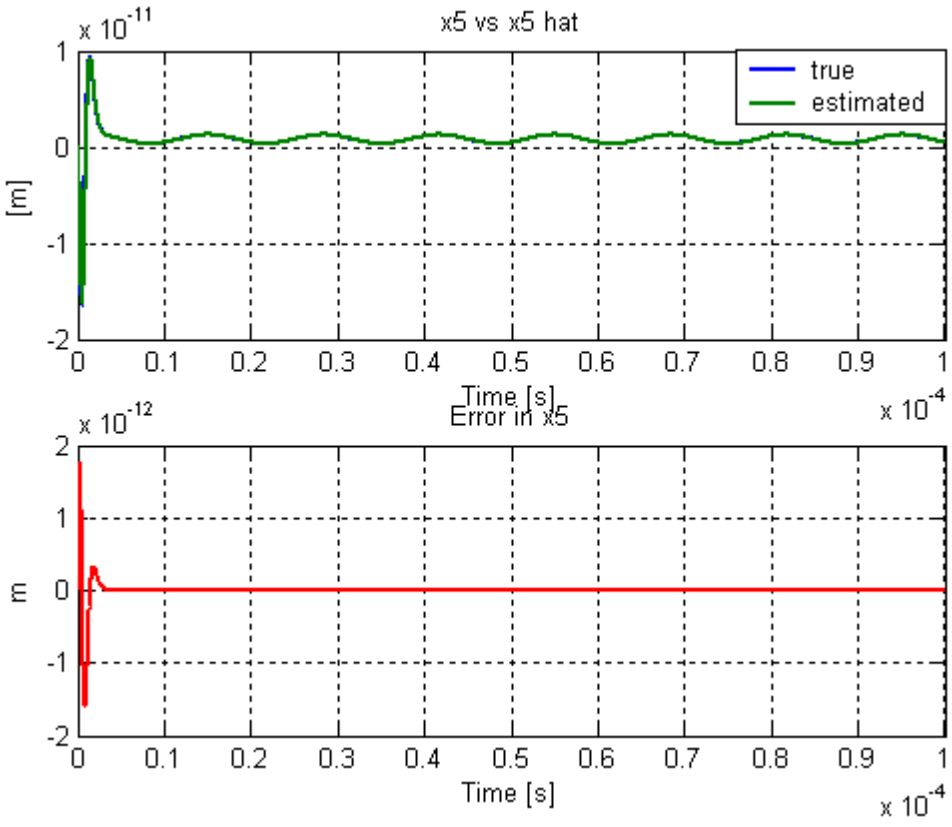

Fig. 23. True and estimated FHM (x_5).

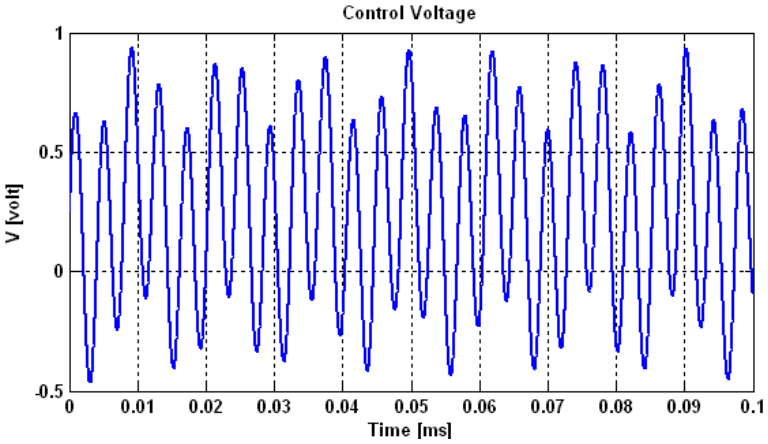

(a) Electrostatic potential 0 V

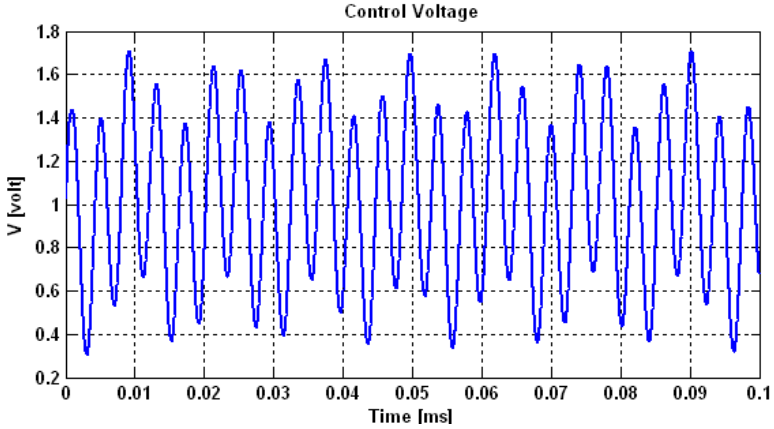

(b) Electrostatic potential 0.5 V

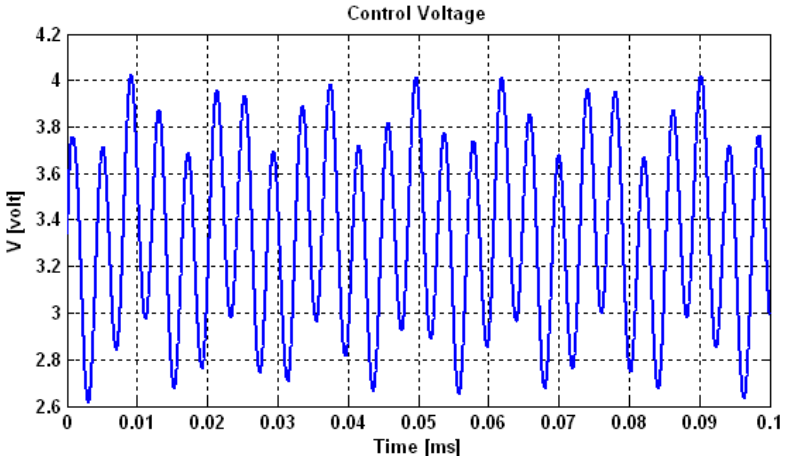

(c) Electrostatic potential 1 V

Fig. 24. Control voltages for different electrostatic potentials. The disk waviness wavelength is 0.2 mm.